Atmospheric
Chemistry
and Physics

Vertical profiles of NO₂, SO₂, HONO, HCHO, CHOCHO and aerosols derived from MAX-DOAS measurements at a rural site in the central western North China Plain and their relation to emission sources and effects of regional transport

Yang Wang[1], Steffen Dörner[1], Sebastian Donner[1], Sebastian Böhnke[1], Isabelle De Smedt[2], Russell R. Dickerson[3], Zipeng Dong[4], Hao He[3], Zhanqing Li[3,4], Zhengqiang Li[5], Donghui Li[5], Dong Liu[6], Xinrong Ren[3,7], Nicolas Theys[7], Yuying Wang[4], Yang Wang[4], Zhenzhu Wang[6], Hua Xu[5], Jiwei Xu[6], and Thomas Wagner[1]

[1]Satellitenfernerkundung, Max-Planck-Institut für Chemie (MPI-C), Mainz, Germany
[2]Belgian Institute for Space Aeronomy (BIRA-IASB), Brussels, Belgium
[3]Department of Atmospheric and Oceanic Science, University of Maryland, College Park, Maryland, USA
[4]College of Global Change and Earth System Sciences, Beijing Normal University, Beijing, China
[5]Institute of Remote Sensing and Digital Earth, Chinese Academy of Sciences, Beijing, China
[6]Key Laboratory of Atmospheric Composition and Optical Radiation, Anhui Institute of Optics and Fine Mechanics, Chinese Academy of Sciences, Hefei, China
[7]Air Resources Laboratory, National Oceanic and Atmospheric Administration, College Park, Maryland, USA

Correspondence: Yang Wang (y.wang@mpic.de)

Abstract. A multi-axis differential optical absorption spectroscopy (MAX-DOAS) instrument was deployed in May and June 2016 at a monitoring station (37.18° N, 114.36° E) in the suburban area of Xingtai, which is one of the most polluted cities in the North China Plain (NCP), during the Atmosphere-Aerosol-Boundary Layer-Cloud (A²BC) experiment and Air chemistry Research In Asia (ARIAs) joint experiments to derive tropospheric vertical profiles of NO₂, SO₂, HONO, HCHO, CHOCHO and aerosols. Aerosol optical depths derived from MAX-DOAS were found to be consistent with collocated sun-photometer measurements. Also the derived near-surface aerosol extinction and HCHO mixing ratio agree well with the coincident visibility meter and in situ HCHO measurements, with mean HCHO near-surface mixing ratios of ∼ 3.5 ppb. Underestimations of MAX-DOAS results compared to in situ measurements of NO₂ (∼ 60 %) and SO₂ (∼ 20 %) are found expectedly due to vertical and horizontal inhomogeneity of trace gases. Vertical profiles of aerosols and NO₂ and SO₂ are reasonably consistent with those measured by a collocated Raman lidar and aircraft spirals over the station. The deviations can be attributed to differences in sensitivity as a function of altitude and substantial horizontal gradients of pollutants. Aerosols, HCHO and CHOCHO profiles typically extended to higher altitudes (with 75 % integrated column located below ∼ 1.4 km) than NO₂, SO₂ and HONO did (with 75 % integrated column below ∼ 0.5 km) under polluted conditions. Lifted layers were systematically observed for all species (except HONO), indicating accumulation, secondary formation or long-range transport of the pollutants at higher altitudes. Maximum values routinely occurred in the morning for NO₂, SO₂ and HONO but occurred at around noon for aerosols, HCHO and CHOCHO, mainly dominated by photochemistry, characteristic upslope–downslope circulation and planetary boundary layer (PBL) dynamics. Significant day-to-day variations are found for all species due to the effect of regional transport and changes in synoptic pattern analysed with the backward propagation approach based on HYSPLIT trajectories. Low pollution was often observed for air masses from the northwest (behind cold fronts), and high pollution was observed from the southern areas such as industrialized Wu'an. The contribution of regional transport for the pollutants measured

at the site during the observation period was estimated to be about 20 % to 30 % for trace gases and about 50 % for aerosols. In addition, agricultural burning events impacted the day-to-day variations in HCHO, CHOCHO and aerosols. It needs to be noted that although several MAX-DOAS measurements of trace gases and aerosols in the NCP area have been reported in previous studies, this study is the first work to derive a comprehensive set of vertical profiles of NO_2, SO_2, HONO, HCHO, CHOCHO and aerosols from measurements of one MAX-DOAS instrument. Also, so far, the validation of MAX-DOAS profile results by comparison with various surface in situ measurements as well as profile measurements from lidar and aircraft is scarce. Moreover, the backward propagation approach for characterizing the contributions of regional transport of pollutants from different regions was applied to the MAX-DOAS results of trace gases and aerosols for the first time.

1 Introduction

The North China Plain (NCP) is one of the most populated, industrialized and economically developed regions in China. The NCP region is located in the northern part of eastern China with an area of about 3 % of the total area of China and with about 20 % of the Chinese population, covering major parts of the provinces Hebei, Henan, Shandong, the northern parts of Anhui and Jiangsu, and the megacities of Beijing and Tianjing. The NCP region is between the Bohai and Huanghai seas to the east and the Taihang Mountains to the west. The Yan Mountains and the Dabie Mountains and Yangtze River delineate northern and southern borders. The main part of the NCP region is shown in Fig. 1. With rapid economic growth and urbanization, air pollution in the NCP region has become severe. The NCP has suffered from the most frequent and severe haze events in China based on the reports from the Ministry of Environmental Protection (MEP, 2017). Previous studies characterized the composition of aerosol particles (e.g. Huang et al., 2014; L. Wang et al., 2012, 2015) and their gaseous precursors (e.g. Ma et al., 2012; Hendrick et al., 2014; Zhu et al., 2016; Jin et al., 2016) to better understand haze events (e.g. Fu et al., 2014). The role of regional transport (e.g. Ding et al., 2009) in haze events has been studied with chemical transport modelling (e.g. L. Wang et al., 2012, 2015) and observations such as ground-based stations, mobile platforms (e.g. Zhu et al., 2016), aircraft (e.g. Ding et al., 2009) and satellites (e.g. Tao et al., 2012). Previous studies demonstrated that secondary aerosols formed through photochemical reactions from trace gas precursors, e.g. nitrogen dioxide (NO_2), sulfur dioxide (SO_2) and volatile organic compounds (VOCs), contribute significantly to aerosols (e.g. Huang et al., 2014). Meteorology (e.g. transport patterns and mixing processes) is also critical for the formation of haze events (e.g. Miao et al., 2015; Wang et al., 2012; Li et al.,

2007). Previous studies were usually based on surface measurements of trace gases and/or column densities derived from satellite observations. Observations of the vertical distribution of trace gases are also important for understanding effects of chemical reactions, their sources and sinks, and the influence of regional transport as well as for validating results from chemical models and satellite observations. EAST-AIRE (East Asian Study of Tropospheric Aerosols: An International Regional Experiment) and associated campaigns generated a number of profiles from aircraft measurements and studied the vertical distribution to help understand the budgets of trace species and to aid in retrievals for remote sensing (Chaudhry et al., 2007; Dickerson et al., 2007; He et al., 2012; Krotkov et al., 2008; C. Li et al., 2010; Z. Q. Li et al., 2007a, b). In addition, airborne measurements were applied to characterize gas and particle pollutants during the CAREBeijing-2008 campaign (Zhang et al., 2014). To date, profile measurements remain scarce.

The multi-axis differential optical absorption spectroscopy (MAX-DOAS) technique, invented about 15 years ago, allows one to derive vertical profiles of trace gases and aerosols in the troposphere from the observation of scattered sunlight at multiple elevation angles (Hönninger and Platt, 2002; Bobrowski et al., 2003; Van Roozendael et al., 2003; Hönninger et al., 2004; Wagner et al., 2004; Wittrock et al., 2004). The existing profile inversion approaches for MAX-DOAS can be sorted into two groups: inversion algorithms based on the optimal estimation (OE) method and iterative approaches, e.g. the Gauß–Newton or Levenberg–Marquardt methods (Rodgers, 2000; Frieß et al., 2006, 2011; Wittrock, 2006; Irie et al., 2008, 2011; Clémer et al., 2010; Yilmaz, 2012; Hartl and Wenig, 2013; Y. Wang et al., 2013a, b), and the so-called parameterized approaches using look-up tables (X. Li et al., 2010, 2013; Vlemmix et al., 2010, 2011; Wagner et al., 2011; Irie et al., 2008, 2011). The MAX-DOAS technique is suitable for long-term observations of trace gases and aerosols with a relative high time resolution of several minutes due to its simple instrument concept, low cost and automatic operation. Several networks of MAX-DOAS instruments have been built to record long-term measurements (e.g. Kanaya et al., 2014). Such measurements, and also data from short-term measurement campaigns, have been used for environmental studies as well as for the validation of satellite observations and model simulations (e.g. Irie et al., 2008; Roscoe et al., 2010; Ma et al., 2013; Kanaya et al., 2014; Vlemmix et al., 2015a; T. Wang et al., 2014; Y. Wang et al., 2017a, b; Hendrick et al., 2014).

Previous studies have reported MAX-DOAS measurements of NO_2, SO_2, nitrous acid (HONO), formaldehyde (HCHO) and glyoxal (CHOCHO) in polluted regions in China (e.g. T. Wang et al., 2014; Hendrick et al., 2014; Y. Wang et al., 2017a; Li et al., 2013; Ma et al., 2013; Schreier et al., 2015). NO_2 and SO_2 can be converted into nitrate and sulfate, and NO_2 contributes to ozone formation. HONO is an important precursor of OH. Recent field mea-
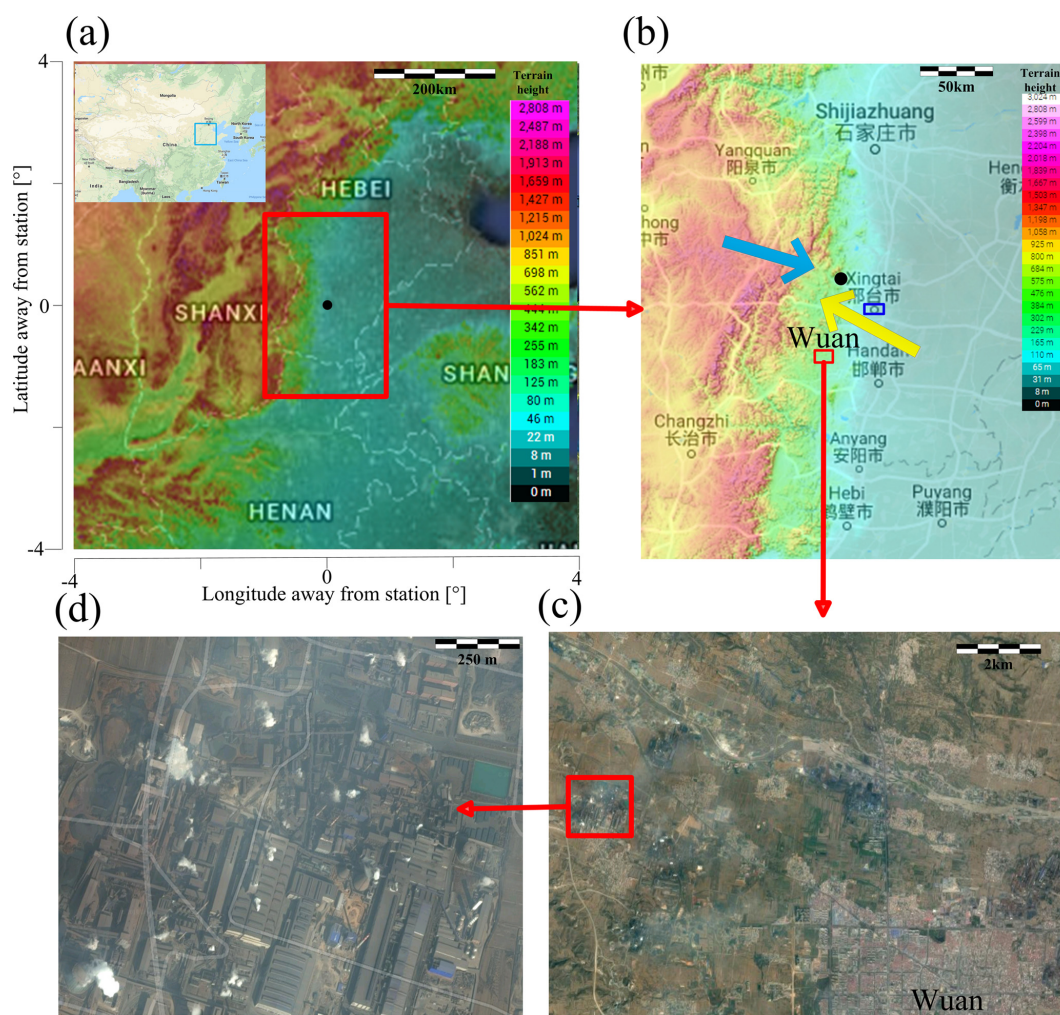
Figure 1. Topography maps (http://en-au.topographic-map.com/places/China-8955742/, last access: 6 April 2019) and satellite images (Google Maps) of the region around the measurement station (37.18° N, 114.37° E), marked in panels **(a)** and **(b)** by black dots. **(a)** Topography map in longitude and latitude ranges of $\pm 4°$ (about ± 360 km) around the measurement station; colours indicate the terrain height, and a map indicating the location of the selected region in China is shown in the top-left corner. **(b)** Topography map of the area marked by the red square in **(a)**; the blue and red squares indicate the areas of Xingtai and Wu'an; the blue (NW wind) and red (SE wind) arrows represent the dominant wind directions before and after 10:00 BT (GMT+8), respectively. **(c)** Satellite image of the area around Wu'an marked by the red square in **(b)**; an industrial area (with many stacks of several iron and coal coking facilities) and the downtown area of Wu'an are located in the north-western and south-eastern parts of the image. **(d)** Zoomed satellite image of one iron and coal coking unit marked by the red square in **(c)**.

surements (e.g. Su et al., 2008, 2011; Li et al., 2014, and references therein) suggest that the observed daytime HONO concentrations cannot be explained by the gas-phase reaction of NO with OH (Stuhl and Niki, 1972; Pagsberg et al., 1997); primary emissions of HCHO could be important in industrial regions (Chen et al., 2014). HCHO and CHOCHO are mainly produced through the oxidation of VOCs, thus their high concentrations indicate photochemical activity. VOCs impact the formation of ozone and organic aerosols. CHOCHO and HCHO have different VOC precursors and different formation pathways (e.g. Vrekoussis et al., 2010; Li et al., 2013).

The Atmosphere-Aerosol-Boundary Layer-Cloud (A^2BC) campaign took place in the heavily polluted southern area of Hebei province from 25 April to 15 June 2016. The aim of the campaign was the investigation of the interaction of gas precursors, aerosols and clouds from ground-based and aircraft measurements. At the Xingtai measurement station in a rural area near the city of Xingtai, we operated a MAX-DOAS instrument developed by the Max Planck Institute for Chemistry (MPIC) to measure vertical profiles of aerosols, NO_2, SO_2, HONO, HCHO and CHOCHO. The southern area of the Hebei province around the Xingtai station is in the central western part of the NCP and contains several cities ranked

among the most polluted in China (based on reports from the Ministry of Environmental Protection), such as Xingtai, Shijiazhuang, Baoding, Tangshan and Handan. The city of Xingtai, with a population of about 7 million, is frequently ranked as China's most polluted city (MEP, 2017). The Taihang Mountains at the western edge of the NCP are 30 km away from the Xingtai station. Previous studies demonstrated the effects of the Taihang Mountains on the accumulation and dispersion of aerosols (e.g. Wei et al., 2010; Miao et al., 2015; L. Wang et al., 2015). MAX-DOAS measurements at the Xingtai station characterize the vertical distribution and temporal variation in aerosols and trace gases to better understand emission sources and effects of regional transport. The availability of other measurements of air pollutants during the campaign enhances the MAX-DOAS results. Spiral up–down aircraft measurements of trace gases and aerosols over the Xingtai station can be used to evaluate the vertical profiles retrieved from the MAX-DOAS measurements. MAX-DOAS results can also be compared with surface concentrations derived from in situ measurements, aerosol optical depths (AODs) measured by a sun photometer, and vertical profiles of aerosol extinction measured by a Raman lidar. In parallel to A^{2}BC, the ARIAs campaign (Air chemistry Research In Asia) investigated trace gases, aerosols and cloud interactions over Hebei (F. Wang et al., 2018; Benish et al., 2019). These and satellite monitoring (Li et al., 2017) indicate a distinct downward trend in SO$_2$ over China recently. Note that although several MAX-DOAS measurements of trace gases and aerosols in the NCP area have been reported in previous studies, this study is the first work to derive a comprehensive set of vertical profiles of NO$_2$, SO$_2$, HONO, HCHO, CHOCHO and aerosols from measurements of one MAX-DOAS instrument. Also, so far, the validation of MAX-DOAS profile results by comparison with various surface in situ measurements as well as profile measurements from the lidar and aircraft is scarce. Moreover, the backward propagation approach to characterize the contributions of regional transport of pollutants from different regions was applied to the MAX-DOAS results of trace gases and aerosols for the first time.

This paper is structured as follows. Section 2 gives an overview of the topography and pollution conditions in the area around the measurement station and the MAX-DOAS measurements. Section 3 introduces other independent measurements and the trajectory simulations. Section 4 presents comparisons of MAX-DOAS results with independent measurements. Effects of regional and local transport of pollutants are discussed in Sect. 5. The conclusions are presented in Sect. 6.

2 MAX-DOAS measurements

2.1 Overview of the measurement station

MAX-DOAS measurements were performed during the A^{2}BC campaign at a station on the central western edge of the NCP area (37.18° N, 114.37° E). Figure 1a indicates the station in the southern area of the Hebei province surrounded by the provinces Shandong, Henan, and Shanxi. The Taihang Mountains are ∼ 30 km west of the station. The terrain height increases from ∼ 10 m a.s.l. to ∼ 1 km a.s.l. in the foothills of the Taihang Mountains. The terrain height of the station is ∼ 200 m a.s.l. Winds from the mountains occurred frequently near the station during the measurement period. Information on wind speed and direction derived from a local weather station is shown in Fig. S1 in the Supplement. Surface winds reflect midday upslope (south-east) and night-time downslope (north-west) circulation. Minimum wind speeds occur usually in a period between about ∼ 08:00 and 10:00 Beijing time (BT; GMT+8 h; all times mentioned in the paper refer to Beijing time). Since the longitude difference of the station and Beijing is only 2°, Beijing time is almost the local time.

Figure 1b indicates the downtown area of Xingtai, with about 7 million inhabitants, located ∼ 20 km south-east of the station. A steel mill is located south-west of the Xingtai downtown area. A large industrial area with several steel and coal coking facilities is located near the city of Wu'an, ∼ 50 km south and south-east of the measurement station. A satellite image of the industrial area derived from the Google Maps service (https://www.google.de/maps, last access: 6 April 2019) is shown in Fig. 1c, and a zoomed image of one of the factories (Fig. 1d) shows many stacks.

Averaged maps of NO$_2$ (from DOMINO v2; Boersma et al., 2007, 2011), SO$_2$ (from BIRA-IASB, Theys et al., 2015) and HCHO (from BIRA-IASB, De Smedt et al., 2008, 2012, 2015) derived from satellite observations of the ozone monitoring instrument (OMI; Levelt et al., 2006a, b) for May and June during the period 2012 to 2016 for the same area as shown in Fig. 1a are shown in Fig. 2a, b and c, respectively. The spatial resolution of the OMI data is 13 km × 24 km in the nadir. Note that the OMI data of the outermost pixels (i.e. pixel numbers 1–5 and 56–60) and pixels affected by the so-called "row anomaly" (see http://www.temis.nl/airpollution/no2col/warning.html, last access: 6 April 2019) were removed. In Fig. 2d a map of the averaged aerosol optical depths (AODs) at 550 nm derived from the Moderate Resolution Imaging Spectroradiometer (MODIS; Kaufman et al., 2002) for the same period is shown (provided by NASA on http://ladsweb.nascom.nasa.gov, last access: 6 April 2019). The spatial resolution of the MODIS AOD data is 5 km × 5 km. In order to exclude cloud-contaminated data for both OMI and MODIS data, only the data with cloud fractions smaller than 30 % are included for the generation of the maps. A grid interval of 0.02° is used to generate the averaged maps of the OMI and MODIS data by binning the

satellite data of pixels around each grid with distance weightings. It is obvious that Fig. 2 indicates strong decreases of all four pollutants along the Taihang Mountains at a line from north-west to south-east. The measurement station is located in the polluted region but close to its edge. The patterns of HCHO and AOD are more homogenous than NO_2 and SO_2. Large values of NO_2, SO_2 and AOD can especially be found in the heavily industrial Wu'an area. High amounts of NO_2 and AOD, but not SO_2, can be seen in the north of the station at a distance of about 100 km around Shijiazhuang, the capital of the Hebei province with about 11 million habitants.

2.2 Operation and processing of MAX-DOAS measurements

2.2.1 Measurement operation

A Tube MAX-DOAS instrument (Donner, 2016) developed by MPIC, Mainz, Germany, was operated at the measurement station during the period from 8 May to 10 June 2016. More details about the instrument can be found in Donner (2016). Spectra of scattered sunlight were routinely recorded by the MAX-DOAS instrument at 11 elevation angles (1, 2, 3, 4, 6, 8, 10, 15, 20, 30 and 90°) in the wavelength range of 300 to 466 nm and with a spectral resolution of about 0.6 nm. The telescope was pointed to the azimuth angle of 25° north-east. The exposure time of each individual spectrum was $\sim$ 1 min. Electric offset and dark current are corrected using background measurements taken at night.

2.2.2 DOAS retrievals of slant column densities

Differential slant column densities (dSCDs; the integrated trace gas number density along the effective light path) of NO_2, SO_2, HCHO, HONO and CHOCHO, and the oxygen dimer (O_4) are retrieved from the recorded spectra using the DOAS technique (Platt and Stutz, 2008). The analysis is implemented using the QDOAS software (http://uv-vis. aeronomie.be/software/QDOAS/, last access: 6 April 2019; Danckaert et al., 2017). The DOAS retrievals are configured based on previous studies, e.g. Wang et al. (2017a, c) and the MAD-CAT campaign (http://joseba.mpch-mainz. mpg.de/mad_analysis.htm, last access: 6 April 2019). The settings are listed in Table 1. A sequential Fraunhofer reference spectrum, which is derived from interpolation of two zenith spectra measured before and after an elevation sequence to the measurement time of individual off-zenith measurements, is used in the DOAS fits. A spectrum measured in the zenith direction closest in time to the off-zenith measurements is used as a Fraunhofer reference spectrum. Typical examples of DOAS fits of the six species are given in Fig. 3. The root-mean square (RMS) of the optical depth of the fit residuals is typically around 6×10^{-4} for O_4, NO_2, HCHO and HONO; 2×10^{-4} for CHOCHO; and 1×10^{-3} for SO_2. The detection limits for the dSCDs are estimated

based on the typical DOAS fit errors of individual species and are about 2×10^{15}, 6×10^{15}, 3×10^{15}, 1×10^{15} and 4×10^{14} molecules cm^{-2} for NO_2, SO_2, HCHO, HONO and CHOCHO, respectively, and 6×10^{41} molecules^2 cm^{-5} for O_4 under typical measurement conditions.

2.2.3 Retrieval of vertical profiles, near-surface values and vertical column densities

Tropospheric vertical profiles of aerosol extinction and volume mixing ratios (VMRs) of NO_2, SO_2, HONO, HCHO, and CHOCHO are retrieved from the elevation-dependent dSCDs by using the PriAM profile inversion algorithm (Wang et al., 2013a, b, 2017a) with a vertical grid of 200 m in an altitude range of up to 4 km. From the derived profiles the vertical column densities (VCDs) of the trace gases and AODs are derived by vertical integrations. Due to the fact that no substantial information on the concentrations above 3 km can be derived from the measurements, the retrieved profiles below 3 km are shown in all figures of the study. The PriAM algorithm is based on the optimal estimation method (Rodgers, 2000) using the radiative transfer model (RTM) of SCIATRAN version 2.2 (Rozanov et al., 2005). The inversion consists of two steps. First, vertical profiles of aerosol extinctions are retrieved from the measured O_4 dSCDs; second, the retrieved aerosol profiles are used for the inversion of the trace gas profiles. For the radiative transfer simulations, the surface height and surface albedo are set as 150 m a.s.l. and 0.05, respectively. A fixed single-scattering albedo (SSA) of 0.95 and an aerosol phase function parameterized according to Henyey and Greenstein (1941) with an asymmetry parameter of 0.72 are chosen according to averaged inversion results at 440 nm from the sun photometer also operated at the measurement station. While F. Wang et al. (2018) reported an averaged SSA of 0.85 at 550 nm based on aircraft observations (Li et al., 2015; Han et al., 2017), the differences between aircraft and the sun-photometer measurements are not currently understood. A systematic bias of the SSA typically contributes to an uncertainty of about 5 % to the retrieved aerosol and trace gas profiles from MAX-DOAS measurements. These values were derived from sensitivity tests by varying SSA in the profile inversion. It needs to be clarified that considering uncertainties of inversions of the SSA and asymmetry parameters of sun-photometer measurements, average values of both parameters are used in the inversion of MAX-DOAS measurements.

Retrieved aerosol extinction profiles at 360 nm are converted into those at 313, 339 and 354 nm for RTM simulations of air mass factors of SO_2, HCHO and HONO, respectively, using an Ångström exponent of 1, which is an average value derived from all the measurements of a collocated sun photometer during the whole campaign. Details of the collocated sun photometer are given in Sect. 3.1.1. The air mass factors simulated by the RTM are used for the profile inversion, and the simulation wavelengths are calcu-

Table 1. Settings used for the O$_4$, NO$_2$, SO$_2$, HCHO and CHOCHO DOAS analyses. Note that the settings for O$_4$, NO$_2$, SO$_2$, and HCHO follow the suggestions in Wang et al. (2017a). The settings for HONO and CHOCHO follow the suggestions in Wang et al. (2017c) and the MAD-CAT campaign (Ortega et al., 2015), respectively.

Parameter	Source	Species					
		O$_4$	NO$_2$	SO$_2$	HCHO	HONO	CHOCHO
Fitting spectral range		351–390 nm	351–390 nm	307.8–330 nm	324.6–359 nm	335–373 nm	400–460 nm
Cross section	NO$_2$: Vandaele et al. (1998), 220, 298 K	×	×	× (only 298 K)	× (only 298 K), I_0 corrected[a] (10^{17} molecules cm^{-2})	× I_0 corrected[a] (10^{17} molecules cm^{-2}); Taylor terms[b] with respect to σ_{NO_2} at 298 K: $\lambda\sigma_{NO_2}$, $\sigma^2_{NO_2}$	× I_0 corrected[a] (10^{17} molecules cm^{-2}); Taylor terms[b] with respect to σ_{NO_2} at 298 K: $\lambda\sigma_{NO_2}$, $\sigma^2_{NO_2}$
	O$_3$: Bogumil et al. (2003), 223 and 243 K		× (only 223 K)	×	×	×	
	O$_4$: Thalman and Volkamer (2013), 293 K	×	×	×	× I_0 corrected[a] (10^{18} molecules cm^{-2})	×	×
	SO$_2$: Bogumil et al. (2003), 293 K			×	×		
	HCHO: Meller and Moortgat (2000), 293 K		×	×	×	×	
	HONO: Stutz et al. (2000), 296 K					×	
	H$_2$O (vapour): Polyansky et al. (2018)					×	×
Ring	Ring spectrum calculated from DOASIS (Kraus, 2006) and additional ring multiplied by λ^{-4} (Wagner et al., 2009)	×	×	×	×	×	×
Intensity offset		Constant	Constant	Constant	Constant	Constant	Constant
Polynomial degree		3	3	5	5	5	5
		Polynomial of order 1 (corresponding to two coefficients)	Polynomial of order 1 (corresponding to two coefficients)

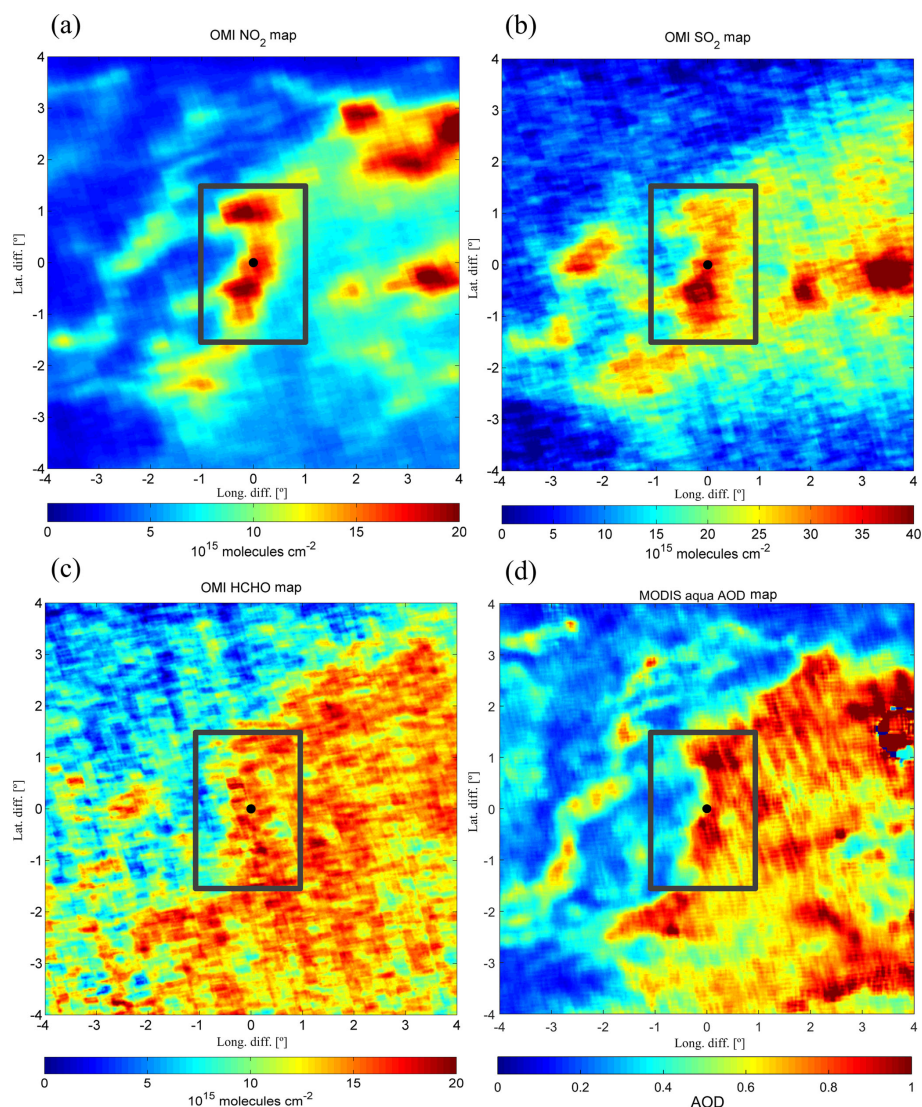[a] Solar I_0 correction from Aliwell et al. (2002). [b] Pukīte et al. (2010).

Figure 2. Maps of average tropospheric VCDs of **(a)** NO_2 from DOMINO v2 (Boersma et al., 2007, 2011), **(b)** SO_2 (Theys et al., 2015) and **(c)** HCHO (De Smedt et al., 2008, 2012, 2015) from BIRA-IASB, derived from OMI observations. Average AODs derived from the MODIS AQUA instrument are shown in **(d)**. The maps show the same area over Eastern China as shown in Fig. 1a. Data are averaged for May and June of all years from 2012 to 2016. The black dots indicate the measurement station. The grey squares mark the same area as shown in Fig. 1b.

lated by weighting the wavelengths by the differential absorption cross section within the individual spectral ranges of the DOAS fits based on the method elaborated in the previous studies, e.g. Marquard et al. (2000). In addition, the uncertainty of the Ångström exponent (due to uncertainties of sun-photometer measurements) typically contributes to uncertainties of up to 20 % to the retrievals of trace gas profiles. These results are derived from sensitivity tests by varying the Ångström exponent from 0.49 to 2.53 in the profile inversion. For the assumed range of the Ångström exponent, see the discussion in Sect. 3.1.1. Temperature and pressure profiles are derived from the MPIC climatological database. Different a priori profiles are used for the individual species according to

previous studies (Wang et al., 2017a; Hendrick et al., 2014) and/or sensitivity tests using different a priori profiles. The a priori profiles are shown as the grey curves in Fig. 4d. The diagonal elements of the a priori covariances (S_a) at different altitudes are set as the square of 100 % of the a priori values at individual altitudes in order to balance the flexibility and stability of the profile inversion.

One indicator for the confidence of the profile inversion is the consistency of the measured and modelled dSCDs (dSCDs simulated by the RTM SCIATRAN for the retrieved profiles). For a systematic analysis, we screened the suspicious profile results with larger differences of measured and modelled dSCDs than the thresholds listed in Table 2. Af-
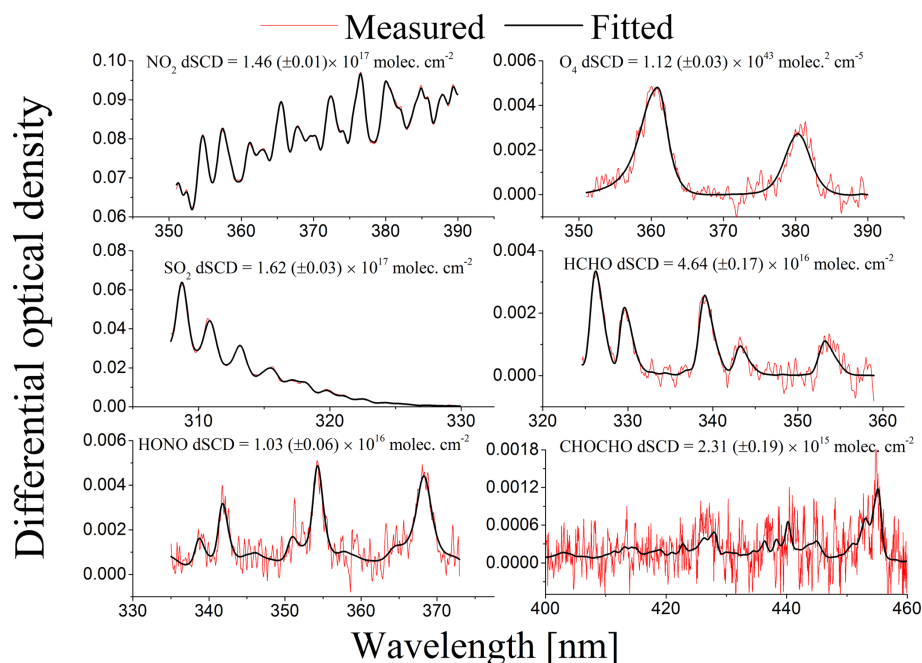
Figure 3. Examples of typical DOAS fits of NO_2, O_4, SO_2, HCHO and HONO at around noon on 17 May and CHOCHO on 27 May 2016. The black and red curves indicate the fitted absorption structures and the derived absorption structures from the measured spectra, respectively. The fitted dSCDs (and fit errors in brackets) are given in the individual subpanels. Note that the CHOCHO fit shown in the figure is for the largest CHOCHO dSCD retrieved at around noon during the whole campaign period.

ter the filtering, the scatter plots, correlation coefficients (R) and slopes derived from linear regressions of the measured against the modelled dSCDs for the different species during the entire measurement period are given in Fig. S2 in the Supplement. The correlation coefficients R are higher than 0.95, and the slopes deviate from unity by less than 2 % for all species.

On 11 May 2016, a typical day with high pollution was selected to show MAX-DOAS results for polluted conditions. Time series of retrieved profiles from the MAX-DOAS measurements on 11 May 2016 are shown in Fig. 4b, and selected profiles at around noon are plotted in Fig. 4d. Note that profiles shown in Fig. 4b are not screened based on the differences of modelled and measured dSCDs. However, the black dots at the top of each panel of Fig. 4b indicate the confident results that remain after filtering). In Fig. 4b a large variability in profile shapes and absolute values can be seen, especially at altitudes below 1 km. The vertical resolution and sensitivities of the retrievals at different altitudes can be quantified by the so-called averaging kernel matrix $\mathbf{AK} = \partial x^{\wedge}/\partial x$, which represents the sensitivity of the retrieved profile $x^{\wedge}$ as a function of the true atmospheric profile x. The typical $\mathbf{AK}$ of the profile inversions shown in Fig. 4c indicates that the sensitivity of the profile retrievals of trace gases and aerosols systematically decreases with altitude.

2.2.4 Cloud classifications from MAX-DOAS measurements

Since clouds can strongly impact the MAX-DOAS results, different sky conditions are identified from the MAX-DOAS observations of the colour index, which is ratio of intensities of sunlight at 330 nm against to at 390 nm and its temporal variations and elevation angle dependences using the cloud classification scheme with certain thresholds. The scheme is developed in Wagner et al. (2014, 2016) and verified in Y. Wang et al. (2015) by comparing with coincident independent ground-based and satellite measurements of clouds and aerosols. The scheme assigns individual MAX-DOAS measurements to one of the five dominant sky condition categories, "cloud-free and low aerosol load", "cloud-free and high aerosol load", "cloud holes", "broken clouds" and "continuous clouds", based on measurements of the colour index. Additionally, some of measurements are assigned to a secondary category of "optically thick clouds" based on MAX-DOAS measurements of O_4 absorptions. The derived sky conditions are indicated by the coloured dots in Fig. 4a. Based on the study by Wang et al. (2017a), cloud-contaminated results of aerosol profiles and AODs are not included in the further analysis; but for all other MAX-DOAS results (including all trace gas results and near-surface aerosol extinctions), only the data under the optically thick clouds condition are skipped. Here it needs to be noted that clouds, especially broken clouds, can impact
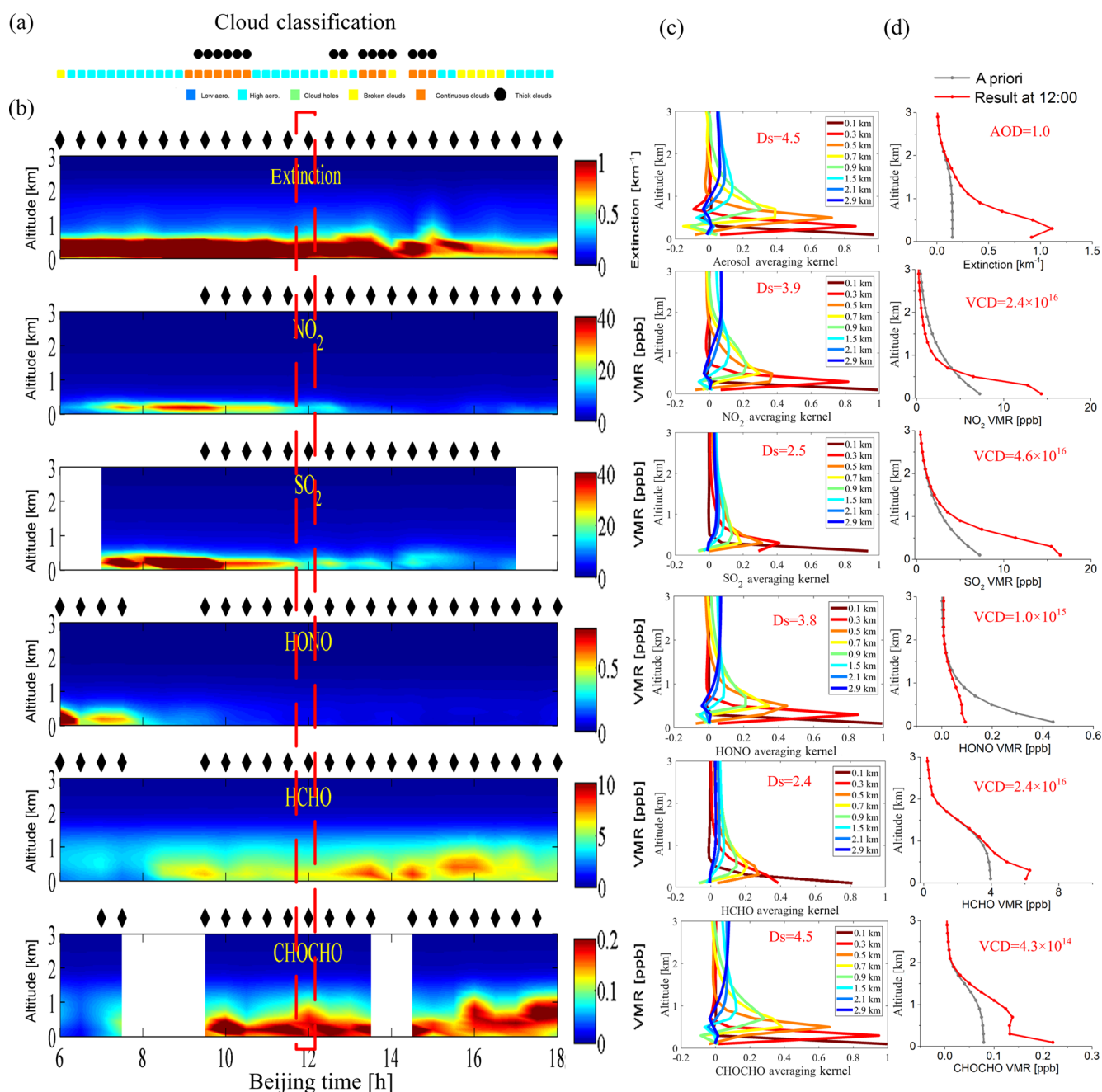
Figure 4. Examples of results derived from MAX-DOAS measurements on 11 May 2016 (with high pollution levels). **(a)** Cloud classification results. **(b)** Time series of vertical profiles of aerosol extinction (including cloud-contaminated results), NO_2, SO_2, HONO, HCHO and CHOCHO VMRs. The black rhombuses (diamonds) plotted above individual subfigures mark "high confidence profiles" (results with deviations between measured and simulated dSCDs smaller than the individual thresholds; see Table 2). **(c)** Averaging kernels (**AK**) of profile retrievals at around noon with information on the degree of freedom (ds). **(d)** A priori profiles and retrieved profiles (with corresponding VCDs) at around noon.

the MAX-DOAS results of the near-surface aerosol extinction for individual measurements. However since the cloud effects occur for different elevation angles, their overall impact is rather random. Therefore if long-term measurements are averaged, cloud effects on the near-surface aerosol mostly

cancel out and do not contribute to a systematic bias (Wang et al., 2017a).

Since certain thresholds are used for the identification of cloud scenarios, two sky conditions might be interchanged because the derived quantities are close to the chosen thresh-

Table 2. Different filters and corresponding thresholds applied to the MAX-DOAS results. The thresholds are experientially determined to exclude most outliers. Also the corresponding fractions of remaining data are indicated (SZA is solar zenith angle; RIO is relative intensity offset in the DOAS fit; RMS is root-mean square of the residual in the DOAS fit).

	Aerosols (O_4)	NO_2	SO_2	HCHO	HONO	CHOCHO
SZA	$< 85\,°$	$< 85\,°$	$< 70\,°$	$< 85\,°$	$< 85\,°$	$< 85\,°$
RIO	$< \pm 1\,\%$	$< \pm 1\,\%$	$< \pm 1\,\%$	$< \pm 1\,\%$	$< \pm 1\,\%$	$< \pm 1\,\%$
RMS	< 0.002	< 0.002	< 0.01	< 0.002	< 0.0012	< 0.001
Deviations of modelled and measured dSCD	$< 2.5 \times 10^{42}$ molecules^2 cm^{-5}	$< 1 \times 10^{16}$ molecules cm^{-2}	$< 1 \times 10^{16}$ molecules cm^{-2}	$< 1 \times 10^{16}$ molecules cm^{-2}	$< 0.8 \times 10^{15}$ molecules cm^{-2}	$< 0.4 \times 10^{15}$ molecules cm^{-2}
Sky condition	Excluding all cloudy conditions	Excluding data under thick cloudy conditions				
Remaining percentage	AOD and profiles: 33 % Near surface: 86 %	62 %	58 %	68 %	57 %	56 %

olds. The problem occurs relatively often between the categories of cloud-free and high aerosol load and continuous clouds because they are only distinguished by the absolute value of the colour index. The issue can impact the MAX-DOAS results of aerosol profiles and AODs due to the remaining cloud contamination. Fortunately the problem can be easily solved if an additional filter is applied, which is the convergence between measured and modelled O_4 dSCDs in the profile inversion for aerosols, based on the previous study in Wagner et al. (2016). If the convergence is bad, the corresponding aerosol results are possibly contaminated by clouds. Therefore the filter of convergence is applied to the MAX-DOAS results for the statistical analysis and elaborated in Sect. 2.2.5 and Table 2.

In addition the issue can also impact the comparisons of MAX-DOAS results with coincident independent measurements under different sky conditions in Sect. 4.1. However since the cases close to the thresholds do not dominate in each category, the general conclusions on the effects of clouds and aerosols are not significantly impacted.

2.2.5 MAX-DOAS results during the entire measurement period

Figure 5 presents an overview of the near-surface values and column densities derived from the MAX-DOAS measurements during the campaign from 8 May to 10 June. To provide some information about the diurnal variation, daily averages for three time intervals of 06:00–10:00 (morning), 10:00–14:00 (noon) and 14:00–18:00 (afternoon) are shown. The corresponding full time series of the MAX-DOAS results for individual days are shown in Fig. S3 in the Supplement. To remove measurements of reduced quality, filters for the solar zenith angle (SZA), relative intensity offset, the RMS of the residuals of the DOAS fits, differences of modelled and measured dSCDs, and sky conditions are applied to the results. The details of the filtering process and thresholds

for different species are shown in Table 2. Here it needs to be noted that a lower SZA threshold is set for the filtering of the SO_2 results than for the other species because the intensity at short wavelengths is rather low and spectral interferences with the O_3 absorption increase strongly with SZA.

Total averaged near-surface aerosol extinctions (0.43 km^{-1}), and VMRs of NO_2 (7.8 ppb), SO_2 (17.1 ppb), HONO (0.22 ppb), HCHO (3.33 ppb) and CHOCHO (0.08 ppb), are shown in Fig. 5, as are AOD (0.65) and VCDs of NO_2 (15.6×10^{15} molecules cm^{-2}), SO_2 (31.7×10^{15} molecules cm^{-2}), HONO (0.21×10^{15} molecules cm^{-2}), HCHO (13.7×10^{15} molecules cm^{-2}) and CHOCHO (0.32×10^{15} molecules cm^{-2}). Rather large day-to-day fluctuations are found for NO_2, SO_2 and HONO, especially in the morning, while the variations for aerosols, HCHO and CHOCHO are smaller. This finding can probably be attributed to transport and the regional nature of secondary pollutants and will be further discussed in Sect. 5. Maximum values for NO_2, SO_2 and HONO frequently occurred in the morning but occurred at around noon for aerosols, HCHO and CHOCHO. Again, this finding can probably be attributed to the different sources and deposition pathways of the different species. NO_2 and SO_2 are removed through reactions with the OH radical, which is more abundant during daytime than during night-time. HONO is rapidly photolysed after sunrise. Therefore maximum concentrations of NO_2, SO_2 and HONO can be expected in the morning, when depth of the planetary boundary layer (PBL) is low and emissions could be high. While CHOCHO and HCHO are also removed via reaction with OH, they can be produced by the reaction of OH with different organic compounds (HCHO can be directly emitted). Because of the high correlation of HCHO and CHOCHO (with R of about 0.94), secondary formation of HCHO is probably the dominant source during the campaign. Typically HCHO and CHOCHO peak at around noon, indicating that the
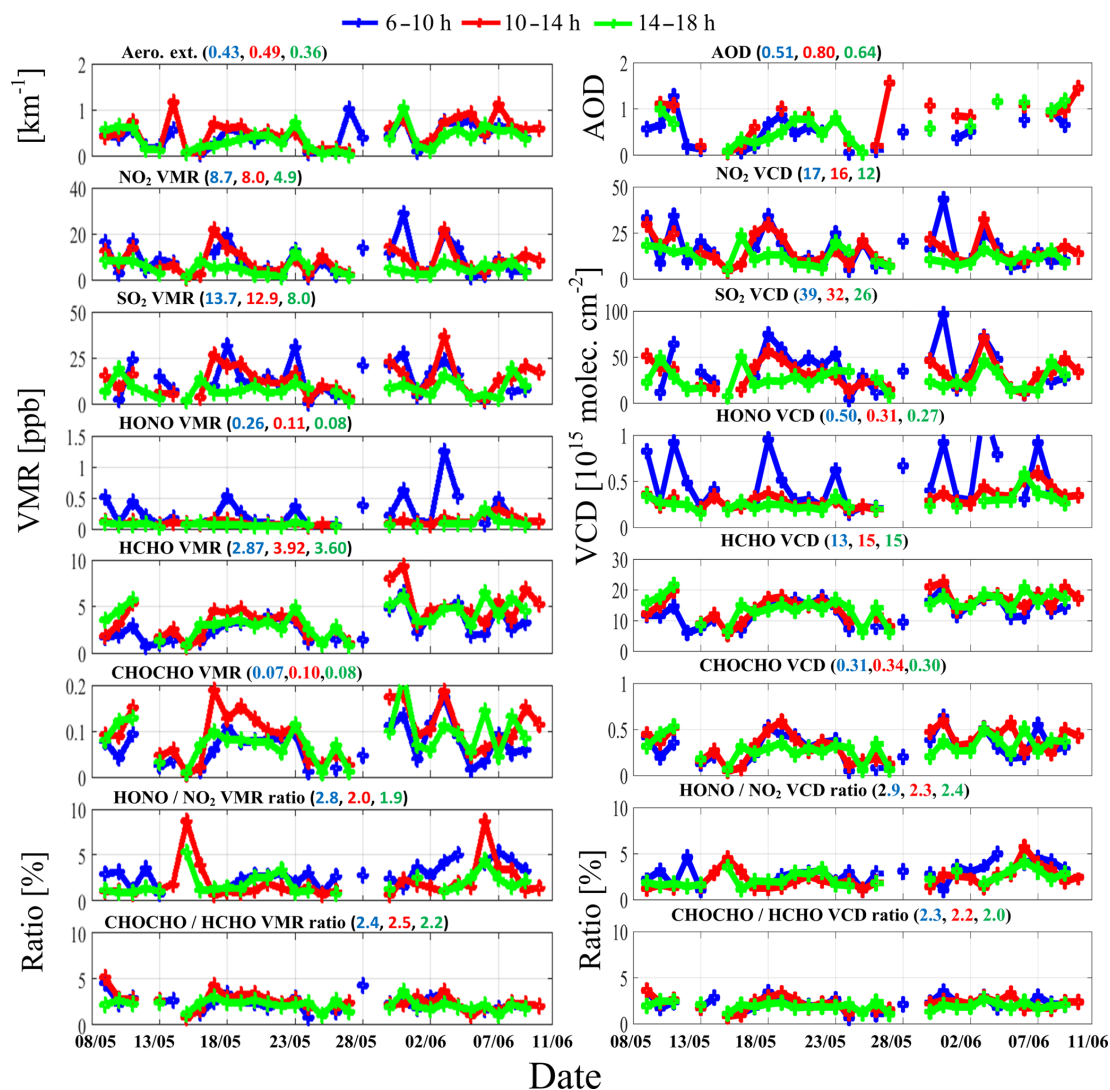
Figure 5. Daily averaged (for three different periods of the day) near-surface aerosol extinction and trace gas VMRs (left), and AODs and trace gas VCDs (right) for the whole campaign. The blue, red and green colours indicate results for the time periods of 06:00–10:00, 10:00–14:00 and 14:00–18:00, respectively. The ratios of HONO versus NO_2 and CHOCHO versus HCHO are also given for the near-surface VMRs (left) and VCDs (right). The colour-coded numbers in the brackets on the top of each subfigure give the averaged values for the different daily periods.

production rate is higher than the loss rate at around noon. For particles, Zhang et al. (2018) also showed that secondary aerosols were dominant in the measurement area based on measurements of an aerosol chemical speciation monitor and a scanning mobility particle sizer located in the measurement station. Since the secondary formation of aerosols also depends on OH radicals, the maximum aerosol formation can be expected at around noon. However, besides the effects of photochemistry, variations in anthropogenic emission rates, effects of local and regional transport, and dispersion can also impact the diurnal variations. These effects will be discussed in more detail in Sect. 5.2.

Consistent day-to-day variations can be found between NO_2, SO_2 and HONO, especially in the morning. We calculate the correlation coefficients (R) between the species because good correlations could imply similar sources and sinks of the species, R values in the morning (in the afternoon) between NO_2 and SO_2, NO_2 and HONO, and SO_2 and HONO are about 0.95 (0.7), 0.73 (0.25) and 0.73 (0.15), respectively. Those between HCHO and CHOCHO are about 0.87, 0.89 and 0.94 in the morning, at around noon and in the afternoon, respectively. Moderate correlations of the day-to-day variations can be found between all the species and aerosols in the morning with an R of 0.6 to 0.7, probably indicating similar sources. In the afternoon, the correlation be-

tween aerosols and with HCHO is up to 0.75, but those with NO_2 and SO_2 are below 0.5, again reflecting the difference between primary and secondary pollutants. A recent study (Zhang et al., 2018) demonstrated that 78 % of PM_1 aerosol particles are secondary aerosols based on the collocated measurements of aerosol composition. They also demonstrated that organic aerosols contribute to about 40 % of the total, consistent with the high correlation between aerosols and HCHO. Sources of the species will be further discussed in Sect. 5.

The correlation between the near-surface and column values is also investigated for the different species. Higher correlations (R) are found for HCHO (0.9) and HONO (0.93) than for aerosols (0.76), NO_2 (0.83) and SO_2 (0.78). The moderate correlations of aerosols, NO_2 and SO_2 could be attributed to the frequent occurrence of the lifted layers (see Fig. 12a, b and c) probably related to transport of pollutants. Remaining cloud effects in the profile inversion after the cloud screenings applied could also partly contribute to the lifted aerosol layers retrieved from MAX-DOAS measurements. The characteristics of the vertical profiles of all species under different situations with different importance of pollution transport will be discussed in Sect. 5.

Ratios of HONO and NO_2 have been often used to characterize possible sources of HONO (e.g. Sörgel et al., 2011a; Wojtal et al., 2011; Li et al., 2012). The day-to-day variations in the HONO/NO_2 ratios (VCDs and VMRs) in the morning, at around noon and in the afternoon are shown in Fig. 5. The ratios are between 1.9 % to 2.9 % on average, with higher ratios in the morning, and are slightly larger than those (0.9 % to 2.4 %) found in spring and summer in Xianghe (a suburban area of Beijing) between 2008 and 2013 (Hendrick et al., 2014). The frequent occurrence of the peak ratio HONO/NO_2 in the morning is consistent with the observation in Xianghe (Hendrick et al., 2014) and could be explained by the faster removal of HONO than of NO_2. Note that Yu et al. (2009) reported HONO/NO_2 ratios of up to 30 % during night-time based on long-path DOAS measurements in Kathmandu, Nepal. Another interesting finding of our study is that on several days (e.g. on 15 May and 6 June), the noon HONO/NO_2 ratios are even up to 10 %. This finding is coincident with low NO_2 values, indicating that the known typical daytime HONO source (gas-phase reaction of NO and OH) cannot explain the observed relatively high HONO values.

Ratios of CHOCHO and HCHO have been used in a number of previous studies to identify sources of VOCs, since CHOCHO and HCHO have different precursors or different formation pathways (e.g. Vrekoussis et al., 2010; Li et al., 2013). The day-to-day variations in the ratios CHO-CHO/HCHO (VCDs and VMRs) in the morning, at around noon and in the afternoon are shown in Fig. 5. They are between 2 % to 2.5 % on average. Similar ratios have been observed at rural sites, e.g. 1.7 % in Nashville, USA (Lee et al., 1998); 3.6 % in Cabauw, the Netherlands (Irie et al., 2011);

and at urban sites, e.g. 3.6 % in Mexico City, Mexico (Lei et al., 2009). However, considerably higher ratios of up to 10 % were also reported in previous studies. For instance, averaged ratios of 6 % to 8 % were derived from the MAX-DOAS measurements in July 2006 in the suburban area of the city of Guangzhou in southern China (Li et al., 2013). The lower ratios derived from our measurements could be (at least partly) related to anthropogenic primary emissions of HCHO. Measurements shown in Benish et al. (2019) also indicate that isoprene, a dominant nature source of secondary HCHO, is not high in the measurement area.

3 Independent data

The MAX-DOAS results are compared to several independent ground-based measurements at the measurement station as well as aircraft measurements over the station. The independent measurements are introduced in Sect. 3.1. For the interpretation of the MAX-DOAS results with respect to transport, we performed backward trajectory simulations and also used the meteorology data from a local weather station. Both data sets are introduced in Sect. 3.2.

3.1 Independent measurements for comparisons with MAX-DOAS results

3.1.1 In situ measurements of NO_x, SO_2, HCHO, sun photometer and visibility meter

An ECOTECH-manufactured in situ gas analyser system measured VMRs of CO, NO, NO_x, SO_2 and O_3 with a time resolution of ~ 3 s during the whole measurement period. NO_2 VMRs are derived by subtracting NO VMRs from NO_x VMRs. For comparisons with MAX-DOAS results, the in situ measurements are averaged over the individual time intervals of the MAX-DOAS measurements.

Surface HCHO VMRs were monitored during the period from 18 to 23 May 2016, using the formaldehyde analyser (Aero-Laser, Germany, Model 4021) based on fluorometric Hantzsch reactions (Gilpin et al., 1997; Rappenglück et al., 2010) with a time resolution of about 1 min. For the comparison with the MAX-DOAS HCHO results, the in situ measurements are averaged over the individual time intervals of the MAX-DOAS measurements.

A sun photometer operated by the Institute of Remote Sensing and Digital Earth, Chinese Academy of Sciences, measures the AODs at eight wavelengths between 340 and 1634 nm. The AODs at 340 and 380 nm are averaged for the comparison with the AODs retrieved from MAX-DOAS measurements at ~ 360 nm. The Ångström parameter, single-scattering albedo and asymmetry factor are also retrieved from the sun-photometer measurements and are used as input for the inversion of the aerosol profiles from MAX-DOAS measurements; for details, see Sect. 2.2.3.

A forward-scattering visibility meter (550 nm) was also operated at the measurement station during the entire measurement period. Aerosol extinction at 360 nm is derived from the visibility at 550 nm using an Ångström exponent of 1, which is the average value derived from the sun-photometer measurements during the whole campaign period. The conversion could contribute a typical uncertainty of up to 20 % due to variability and uncertainties in the Ångström exponent. F. Wang et al. (2018) reported a much higher value for the Ångström exponent: from 0.49 to 2.53 (median 1.53) for the same campaign. These values are based on observations made from the aircraft equipped with an aerosol inlet with a reported 50 % cut-off at 5 µm. The decreased sensitivity for large aerosol particles together with unobserved aerosol below the lowest altitude of the aircraft spirals (∼ 300 m a.g.l.) could contribute to the difference between the aircraft and ground-based sun-photometer measurements. Sun photometers measure AOD directly, and the Ångström exponent is derived from AODs at different wavelengths.

3.1.2 Lidar

A three-wavelength Raman polarization lidar system (Tao et al., 2012; Liu et al., 2013) developed by the Key Laboratory of Atmospheric Composition and Optical Radiation, Hefei Institutes of Physical Science, Chinese Academy of Sciences (CAS), was operated on several days during the campaign. Profiles of aerosol extinctions at 355 nm above 500 m are retrieved from the lidar measurements with a vertical resolution of 7.5 m. There are two mainly cloud-free days (16 and 17 May) on which the lidar measurements overlapped with the MAX-DOAS measurements. Therefore comparisons between MAX-DOAS and lidar are done for these days (Sect. 4.2).

3.1.3 Aircraft measurements

On several days during the measurement period, a Y-12 airplane (twin-engine multipurpose transport aircraft, Harbin Aircraft Manufacturing Corporation) from the Weather Modification Office of the Hebei Meteorological Bureau flew spirals down to about 200 m above the measurement station and other sites to obtain atmospheric profiles of aerosol optical properties and trace gas concentrations (F. Wang et al., 2018; Benish et al., 2019). The diameters of the spiraling circles were about 10 km. The aircraft measurements overlapped with the MAX-DOAS measurements on 8 and 21 May 2016. On the Y-12 airplane, SO_2 was monitored by a commercially available trace-level pulsed fluorescence analyser (TEI Model 43C; Luke, 1997). NO_2 was measured using a modified commercially available cavity ring-down spectroscopy (CRDS) detector (Brent et al., 2013; Castellanos et al., 2009). Aerosol scatterings were measured at 550 nm using an integrating nephelometer (Trust Science Innovation, TSI Model

3563), and aerosol absorptions were measured at 565 nm and converted into those at 550 nm using a particle soot absorption photometer (PSAP; e.g. Anderson et al., 1996; Taubman et al., 2006). All instruments were routinely calibrated during the measurements (Brent et al., 2013; He, 2012; He et al., 2014; Taubman et al., 2006). For the comparison with the MAX-DOAS profiles, the aerosol extinction at 550 nm (the sum of aerosol scattering and absorption) is converted into that at 360 nm using averaged Ångström parameters of 0.8 on 8 May and 1.5 on 21 May derived from the sun-photometer measurements.

3.2 Meteorological data and air mass trajectories

To interpret the measurement results, we derived meteorological parameters, including ambient temperature (T), relative humidity (RH), wind speed (WS), wind direction (WD) and precipitation from the weather station at the measurement station of the MAX-DOAS instrument. The weather station was conducted by the Xingtai Meteorological Administration. For the discussion of the effect of regional transport of pollutants in Sect. 5, we performed 12 h backward trajectory simulations starting at each hour throughout the day and ending at 100 m, 300 m and 1 km above the measurement station, using the HYSPLIT model (Stein et al., 2015) developed by the Air Resources Laboratory of the NOAA (https://ready.arl.noaa.gov/HYSPLIT.php, last access: 11 April 2019). The meteorological data used for the backward trajectory calculation were from the NCEP Global Data Assimilation System (http://www.emc.ncep.noaa.gov/gmb/gdas/, last access: 11 April 2019) with a spatial resolution of 0.5° and a time resolution of 6 h.

4 Comparison of MAX-DOAS results with independent measurements

4.1 Comparison with a sun photometer, visibility meter and in situ measurements

Comparisons of MAX-DOAS aerosol results with co-located independent measurements are done under three different sky condition categories, including "clear sky with low aerosol load", "clear sky with high aerosol load" and "cloudy sky" (optically thick clouds are excluded). The sky conditions are characterized based on MAX-DOAS measurements (see Sect. 2.2.4). The comparison results are shown in Fig. 6 with colours to indicate the time of day.

AODs retrieved by MAX-DOAS measurements are compared with those retrieved from the sun-photometer measurements in Fig. 6a. Because for MAX-DOAS measurements, AOD results are skipped for cloudy conditions (and also sun-photometer measurements are only available for clear sky), no comparison results for cloudy situations are shown in Fig. 6a. For clear-sky observations, better agreement is found for the category low aerosol (R of 0.84 and slope of 1.13)
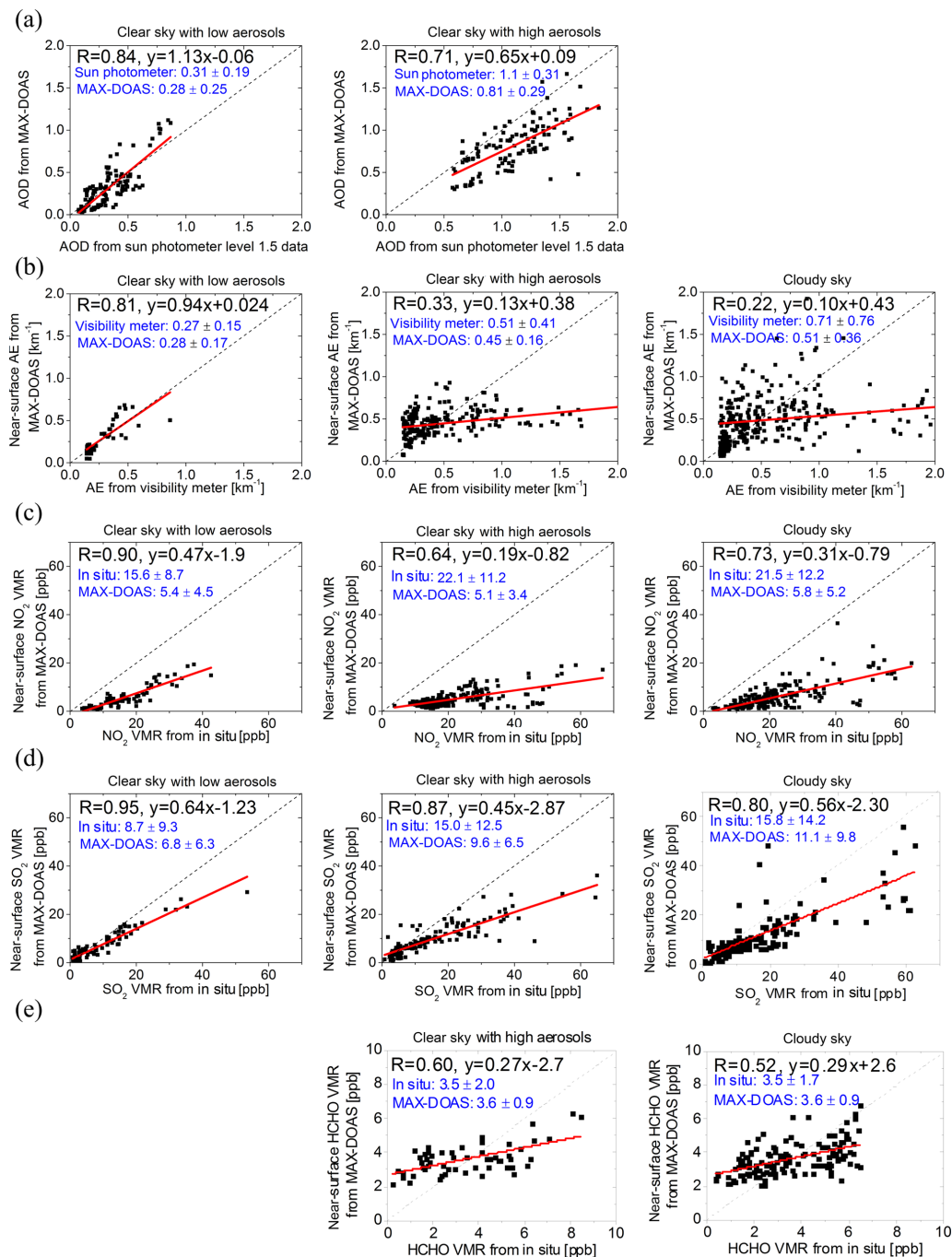
Figure 6. Correlation plots of AODs **(a)**, near-surface aerosol extinction **(b)**, and VMRs of NO_2 **(c)**, SO_2 **(d)** and HCHO **(e)** derived from MAX-DOAS measurements versus results from other techniques. Mean values and standard deviations of the compared values are marked by the blue colour and given before and after $\pm$ in individual subfigures. AODs are taken from the level 1.5 product (cloud-screened and quality-controlled) derived from sun-photometer measurements. Note that the level 2.0 (quality-assured) AOD product is not (yet) available. Near-surface aerosol extinction is derived from visibility meter measurements. Surface VMRs of NO_2, SO_2 and HCHO are derived from the in situ instruments (see Sect. 3). The data of the sun photometer, visibility meter, and in situ measurements of NO_2 and SO_2 during the whole campaign period from 8 May to 10 June 2016 are included in the comparisons. The data of in situ measurements of HCHO during the period from 18 to 23 May are included in the comparisons due to the short-term operations of the in situ instrument. All independent data are averaged over the individual time intervals of the MAX-DOAS measurements.

than for high aerosol (R of 0.71 and slope of 0.65). The a priori constraint in the MAX-DOAS profile inversion is probably the main reason for the underestimation of the AOD under high aerosol conditions. Low sensitivity of MAX-DOAS measurements in aerosols located at high altitudes can also play a role. This finding is illustrated in Fig. 8b and discussed in Sect. 4.3. In addition, the sun photometer measured the air masses in the direction of the sun. The different air masses measured by the two techniques can contribute to the differences of the AOD results. The comparison of the near-surface aerosol extinction between the MAX-DOAS measurements and the visibility meter is shown in Fig. 6b. While very good agreement is found for the category clear sky with low aerosols (R of 0.81 and slope of 1.02), much worse correlation is found for clear sky with high aerosols (R of 0.32 and slope of 0.14). Even worse agreement is found for the category cloudy sky (R of 0.22 and slope of 0.11). The largest underestimation of the MAX-DOAS results compared to the visibility-meter results is found in the morning and when aerosol loads are large. Since the boundary layer height is lower in the morning, larger vertical gradients of aerosols in the layer between 0 and 200 m can be expected. The different air mass measured by the MAX-DOAS and the visibility meter together with strong vertical gradients near the surface might be the reason for the large underestimation of the MAX-DOAS results compared to the visibility-meter results. In addition, the effect of clouds on the MAX-DOAS aerosol retrievals is probably the reason for the larger scattering under the cloudy sky conditions compared to cloud-free sky conditions. Note that clouds are not included in the RTM which is used for profile retrievals of aerosols and trace gases.

The near-surface NO_2 and SO_2 VMRs retrieved from the MAX-DOAS measurements are compared to the in situ measurements (see Sect. 3.1.1) in Fig. 6c and d, respectively. Rather high correlation coefficients are found for both NO_2 (R of 0.9) and SO_2 (R of 0.95) for the category clear sky with low aerosol. Larger scatter is found for the other two sky conditions partly due to cloud effects on the MAX-DOAS profile inversion. Further, different cloud effects on NO_2 and SO_2 comparisons are found. For SO_2 worse correlation is found under cloudy sky conditions than under clear sky with high aerosols, while a better correlation is found for NO_2. Effects of clouds in the profile retrievals of SO_2 can be expected to be stronger than for NO_2 due to the fact that SO_2 can extend to higher altitudes than NO_2, as shown in Fig. 12. In addition, the photolysis rate of NO_2 can be expected to be lower under cloudy conditions than under cloud-free sky conditions. Therefore the vertical distributions of NO_2 in the layer between 0 and 200 m might be smoother under cloudy conditions than under the cloud-free sky condition. The smoother vertical distribution is probably the reason for the better agreement of the NO_2 results between the MAX-DOAS results and in situ measurements. It has, in general, also been found that the MAX-DOAS results are systemati-

cally lower than the in situ results for NO_2 and SO_2 (slopes below unity). This finding is probably related to vertical (especially in the lowest vertical layer between 0 and 200 m) and horizontal inhomogeneity of the species, different air measured by the two techniques, some artefacts of spectral analysis, and profile inversion of MAX-DOAS measurements. In addition interference of NO_y with NO_x in the in situ measurements could cause overestimation of NO_2. This might explain the smaller slope of NO_2 than that of SO_2 in Fig. 6.

The correlation plot of the near-surface HCHO VMRs retrieved from the MAX-DOAS measurements versus those from the in situ HCHO analyser is shown in Fig. 6e. Note that only 1 week of in situ data is available for this comparison. And the category clear sky with low aerosols did not occur in this week. The averaging values are comparable between the two measurements. However, the slopes of ~ 0.3 strongly deviate from unity, similar to other species.

Note that the visibility meter and the in situ measurements of NO_2, SO_2 and HCHO represent air masses close to the instruments, whereas the MAX-DOAS measurements represent averages of pollutants along the effective horizontal light path of ~ 5 to 10 km in the vertical grid from the surface up to 0.2 km. Therefore different probed air masses can be seen as one important reason for the differences of results.

4.2 Comparisons with lidar measurements

In this section profiles of aerosol extinction retrieved from the MAX-DOAS measurements are compared with those derived from the lidar measurements on 2 mostly cloud-free days. Aerosol loads on 16 May are lower than those on 17 May. The comparison of the time series of both selected days is shown in Fig. 7, also including the AODs derived from the MAX-DOAS and the sun-photometer measurements. Note that no aerosol profiles below 500 m are derived from the lidar measurements due to missing overlap between the outgoing beam and the field of view (FOV) of the telescope. In general reasonable agreement of the aerosol profiles from both techniques is found above 500 m. The remaining differences can probably be explained by the fact that different air masses are observed by both techniques, while horizontal inhomogeneities of aerosols and cloud cover could appear. For example, different clouds and aerosols could be observed by both instruments. Note that the MAX-DOAS telescope was pointed towards the north, while the lidar measured the atmosphere directly above the station. The sun photometer measured the air masses in the direction of the sun.

4.3 Comparisons with aircraft measurements

The MAX-DOAS results of vertical profiles of aerosol extinction and NO_2 and SO_2 VMRs are compared to the aircraft measurements over the station at the time interval of 13:30 to 14:00 BT on 8 May 2016 and 12:45 to 13:45 BT on
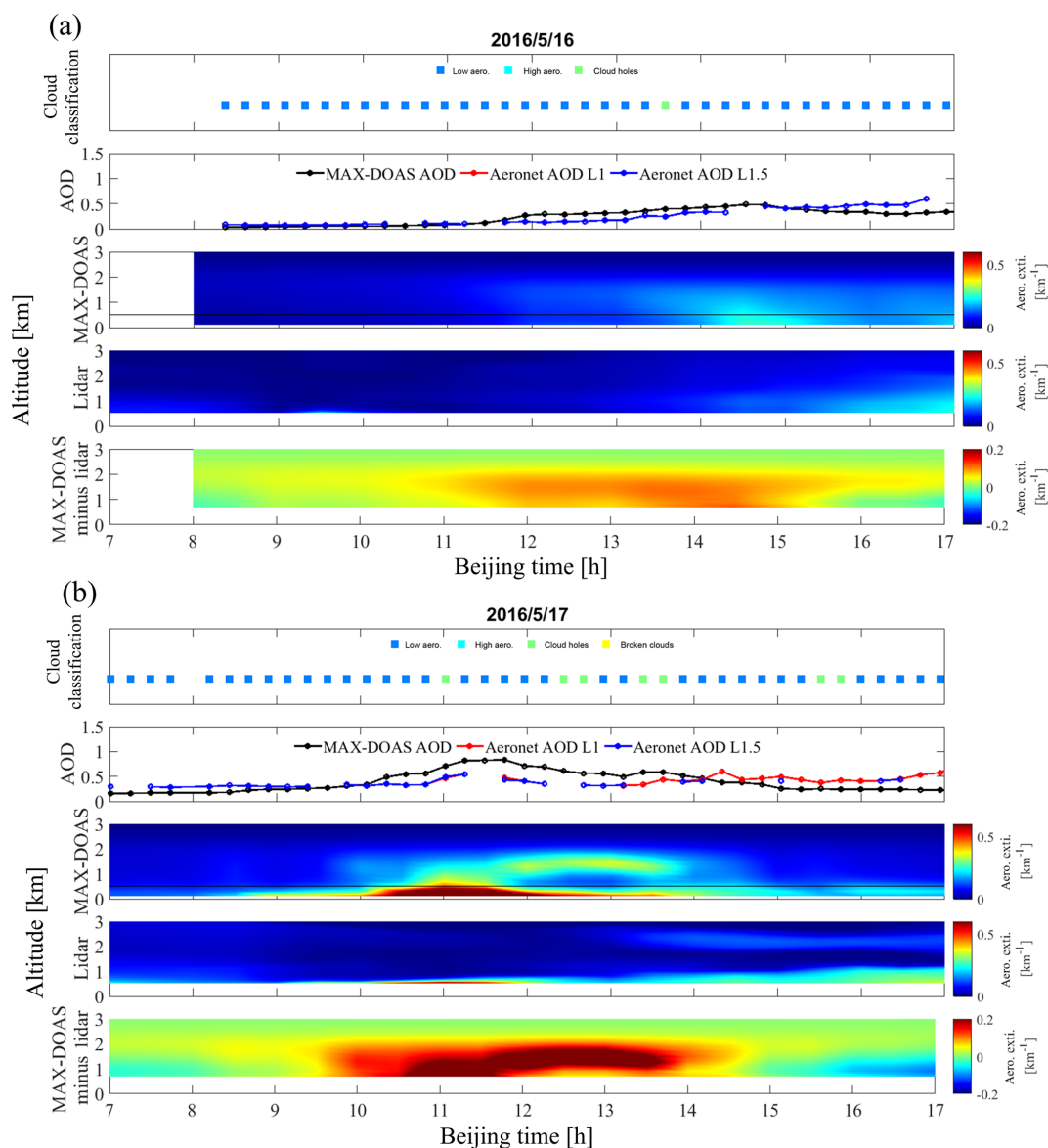
Figure 7. Vertical profiles of aerosol extinctions derived from MAX-DOAS and lidar measurements on 16 May 2016 **(a)** and 17 May 2016 **(b)**. Differences of aerosol extinction results between from MAX-DOAS and lidar measurements are also given at the bottom of both subfigures. Note that colour bar in the plots of differences is different from that in the plots of vertical profiles. Cloud classification results are shown at the top of both subfigures. AODs (black) are derived from the MAX-DOAS measurements and from the sun photometer. The red and blue lines shown in the second row are the level 1 (unscreened) and level 1.5 (cloud-screened and quality-controlled) products, respectively. The black line in the third subpanels in **(a)** and **(b)** marks the lower limit (500 m) of the LIDAR profiles.

21 May 2016. The individual and averaged values of the aircraft measurements as well as the averaged, minimum and maximum profiles derived from the MAX-DOAS measurements during the overpass times of the aircraft are shown in Fig. 8 (also including the surface values measured by co-located independent measurements). "Combined profiles" are generated by combining averaged aircraft profiles with averaged surface measurements. Values at altitudes between the lowest aircraft measurements and surface measurements are generated by linear interpolations. Because of the limited

response of MAX-DOAS profile retrievals to the true profiles, the retrieved profile $x^\wedge$ can be represented as the true profile x, smoothed by the $\mathbf{AK}$ according to the following equation: $x^\wedge = x_a + \mathbf{AK}(x - x_a)$, where x_a is a priori profile used in the profile retrievals of MAX-DOAS. To account for the smoothing effect of the MAX-DOAS profile inversion in the comparisons, the $\mathbf{AK}$ values of the MAX-DOAS profile retrievals are applied to the averaged aircraft profiles, which are treated as the true atmospheric profile x to generate the "smoothed profiles" $x^\wedge$. Additionally, the combined profiles,
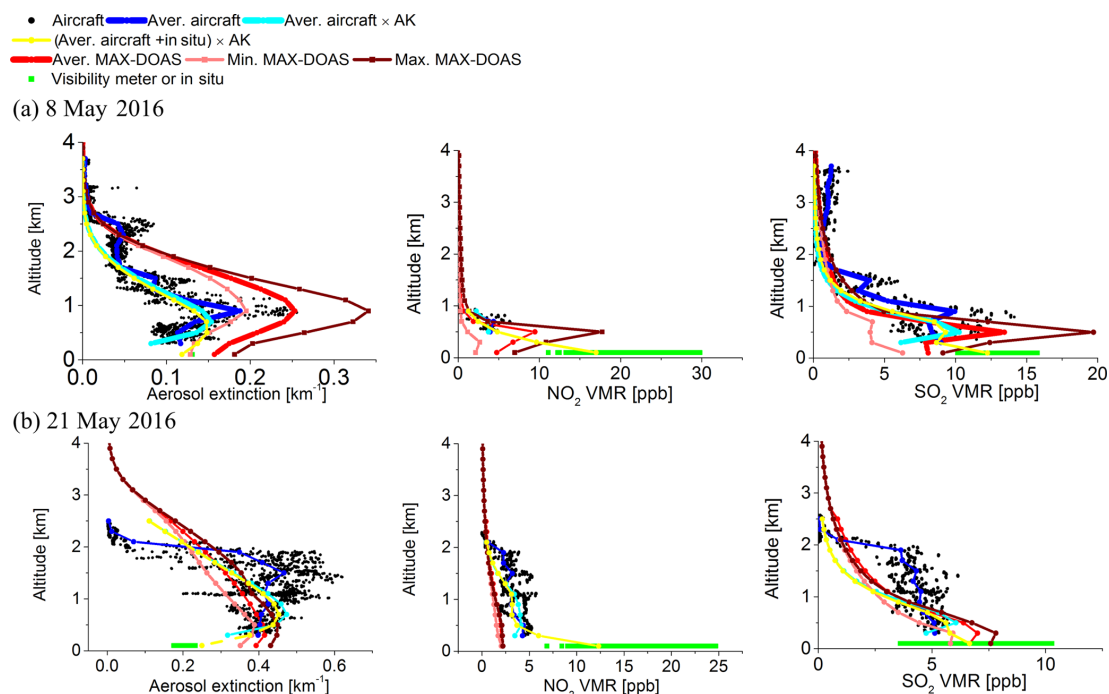
Figure 8. Vertical profiles of aerosol extinction, and VMRs of NO_2 and SO_2 derived from the MAX-DOAS measurements compared with corresponding aircraft measurements on 8 May 2016 **(a)** and 21 May 2016 **(b)**. The black dots represent the original aircraft measurements. The light and dark blue curves show the averaged and smoothed (with the averaging kernels) aircraft data. The red, pink and brown lines indicate the averaged, maximum and minimum profiles derived from the MAX-DOAS measurements during the overpass time of the aircraft measurements. The near-surface values from the visibility meter and in situ trace gas measurements are indicated by the green dots. The yellow curves show the averaged and smoothed combined profiles from aircraft and surface measurements.

derived from the averaged aircraft profile and surface data, are considered to be the true atmospheric profile x and are converted into "smoothed combined profiles" using the AK of the MAX-DOAS profile retrievals. The smoothed profiles and smoothed combined profiles" are shown in Fig. 8. In general the smoothed profiles of all the species agree better with the MAX-DOAS results than the original aircraft profiles. And the values at the height of 300 m in the smoothed combined profiles are often higher than those in the smoothed profiles due to contributions of surface values to high altitudes by the smoothing of the **AK** values. By comparing the smoothed profiles with the original profiles derived from the aircraft measurements, the smoothing effect of MAX-DOAS retrievals can be evaluated. The smoothing effect is especially strong on 21 May. On that day, the box-shaped profiles of aerosols and SO_2 below 2 km are "reshaped" to exponentially decreasing profiles with maxima at about 500 m altitude. Generally, pollutants above 1 km are significantly underestimated due to the smoothing effect of MAX-DOAS profile retrievals. Besides errors of the MAX-DOAS profile inversion, the deviations between the MAX-DOAS and aircraft measurements can probably also be attributed to inhomogeneous horizontal distributions of pollutants and their temporal variation during a period of aircraft measurements. The differences between the maximum and minimum pro-

files from the MAX-DOAS measurements in Fig. 8 indicate the range; the scatter of the original aircraft measurements indicates considerable horizontal gradients within the ~ 10 km diameter of the spirals. In addition, aircraft results represent in situ measurements along the spiral route, whereas MAX-DOAS results represent averages of pollutants over an effective light path of ~ 5 to 10 km. The different air masses measured by the two techniques can be seen as one important reason for the observed differences of the measured results. For NO_2, significantly larger values of the aircraft measurements than the MAX-DOAS measurements can be seen on 21 May. Since the same technique as that for the ground-based in situ measurements of NO_2 (see Sect. 4.1) was used in the aircraft measurements, the interference of NO_y with $NO+_x$ might also cause an overestimation of the NO_2 concentrations derived from the aircraft measurements.

5 Regional and local transport of pollutants

In this section, effects of regional and local transport of pollutants in the measurement area are discussed based on a case study in Sect. 5.1 and a systematic analysis in Sect. 5.2. Possible cleaning effects of pollutants caused by precipitation are also discussed in Sect. 5.1.
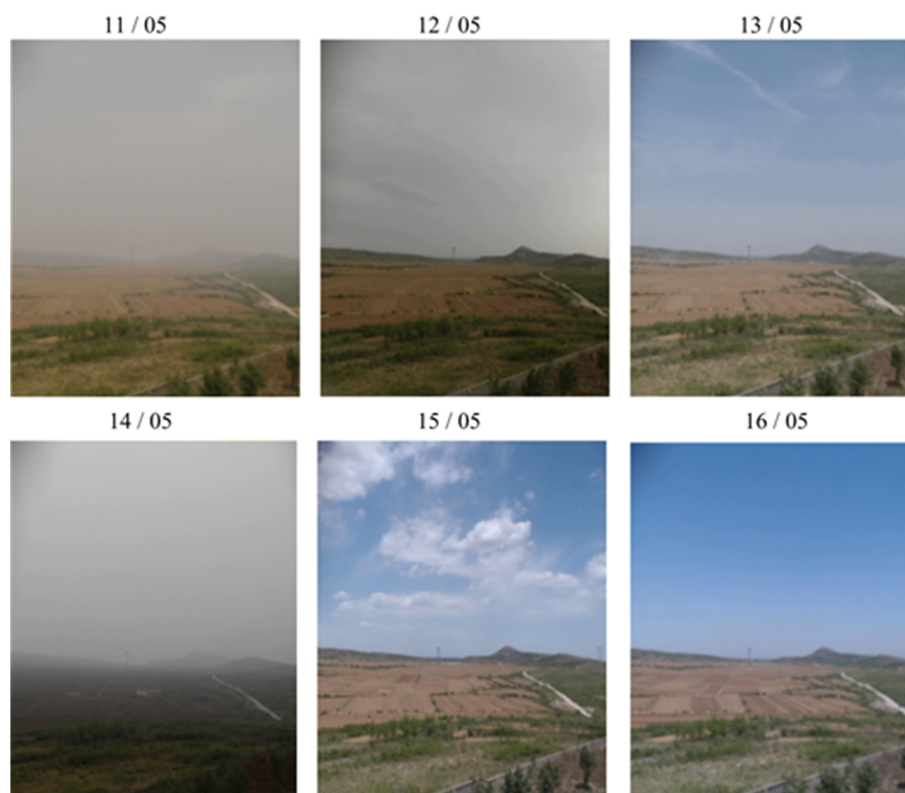
Figure 9. Photos taken by a camera along the line of sight of the MAX-DOAS instrument in the period from 11 to 16 May 2016 (left to right).

5.1 A typical case period

Photos taken by a camera along the line of sight of the MAX-DOAS instrument at around noon on the days from 11 to 16 May 2016 are shown in Fig. 9, indicating different pollution conditions. What happened on these days to result in either blue skies or low visibility (high pollution)? The question will be answered based on regional and local meteorological data and the temporal evolution of the pollutants. The regional transport related to the weather system of cold and warm front from the north-west and south could be the dominant driver for the air quality in the region.

All available data on pollutants and meteorological parameters during the period from 11 to 16 May 2016 are shown in Fig. 10. The corresponding plots for the other days of the campaign are shown in Fig. S3 in the Supplement. Backward trajectories of 12 h ending at 100 m and 1 km over the measurement site in intervals of 1 h are also shown in Fig. 10. The trajectories indicate the regions from which regional transport of air mass will originate at the measurement site. Also surface wind directions and wind speeds are provided in Fig. 10, indicating the origin of local (short-range) transport of air. The mountain-plain topography causes a daily cycle with downslope (north-east winds) and upslope (south-east winds) winds. Hourly accumulated precipitation rates, am-

bient humidity and temperatures are also shown in Fig. 10. Note that trajectories, local winds, precipitation, humidity and temperatures are shown for the full 24 h of each day, while visibility, AOD at 360 nm, surface trace gas VMRs and MAX-DOAS results are only shown for daytime (06:00 to 18:00 BT). The results derived from the MAX-DOAS measurements in Fig. 10 include cloud classification results and vertical profiles of aerosols and trace gases (including cloud-contaminated results). Note that the profiles shown in Fig. 10 are not screened based on the differences of modelled and measured dSCDs (see Table 2) and clouds, but the black dots at the top of each panel of profiles indicate the confident results which have passed the filters described in Table 2. In addition, daily total numbers of fire points derived from the MODIS satellite observations in the NCP area are shown in Fig. 10 in order to show the potential influence of biomass burning.

The results shown in Fig. 10 indicate that aerosols and trace gases steeply decrease from 11 to 12 May. Figure 9 indicates that also the visibility significantly increased from 11 to 12 May. The backward trajectories in Fig. 10 indicate that the origin of air masses arriving at the measurement site changes from the south and south-west to north-west during the night from 11 to 12 May. As shown in Figs. 1 and 2, the area around Wu'an about 50 km south-west of the mea-
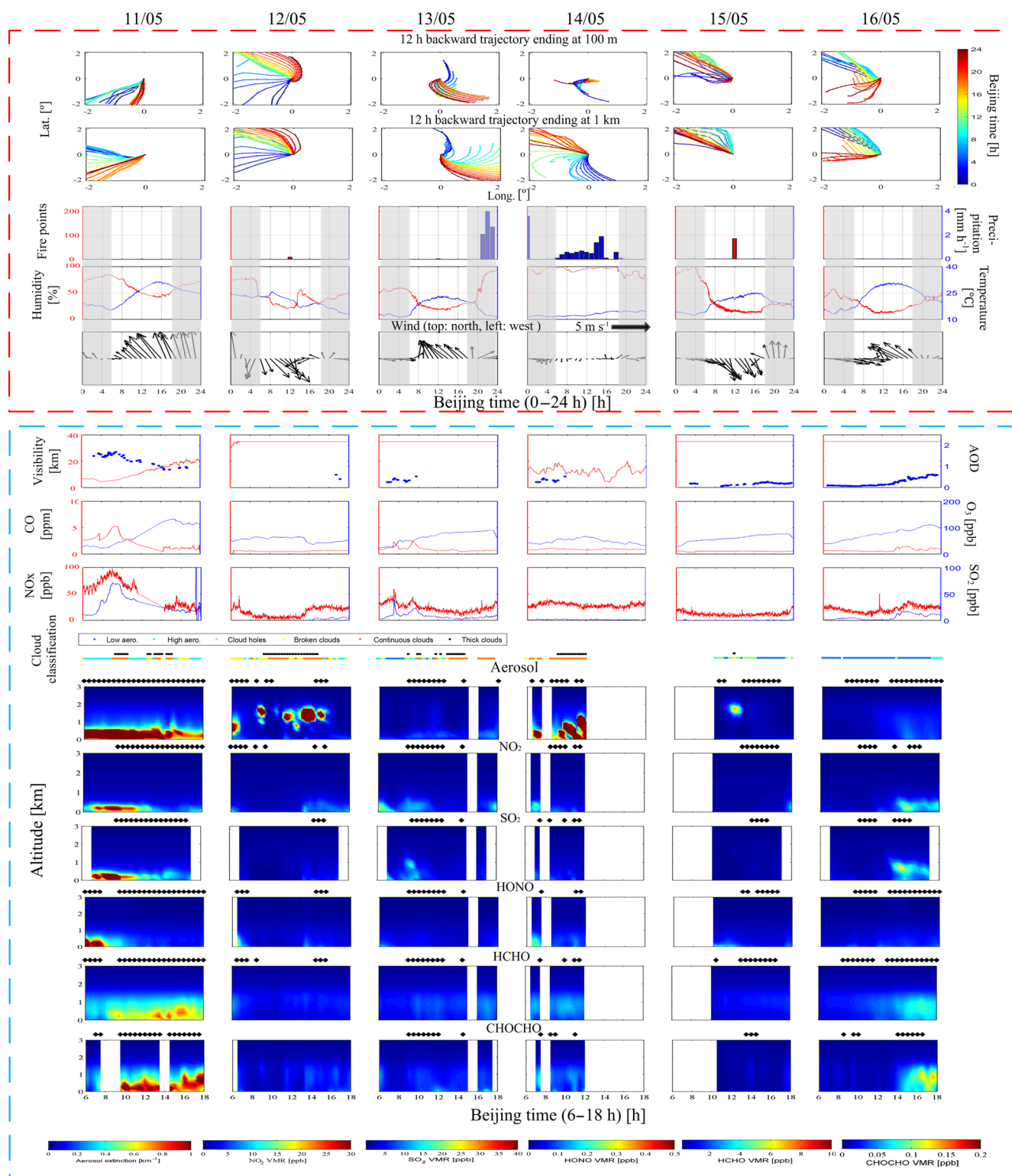
Figure 10. Results from MAX-DOAS measurements, trajectories, meteorological data and independent measurements of pollutants during the period from 11 to 16 May 2016. The figures surrounded by the red and blue dashed boxes show the values for 24 h periods (red) or 12 h (blue) daylight periods (06:00–18:00). The total fire points in the NCP area are derived from MODIS observations and the hourly accumulated precipitation were measured at the station (third row). In the fifth row hourly averaged local winds are given by arrows moving with the wind. The colour bars of the MAX-DOAS profiles are given at the bottom. The black rhombuses plotted above the individual subfigures of the time series of MAX-DOAS profiles mark those that are most reliable (thresholds are given in Table 2).

surement site is significantly polluted due to emissions from many iron and coal coking factories. The high amounts of pollutants observed in the morning on 11 May can be attributed to night-time transport of pollutants from the Wu'an area based on the dominant south-westerly trajectories before sunrise. In contrast, the areas in the other directions, especially in the north-west, are relatively clean. Therefore the cleaning event can be attributed to regional transport of clean air from the north-west.

The 14th was a day of steady, stratiform rain associated with a warm front followed by cold front passage from the north-west. Frontal passage was on the 14th with south-east (SE) winds ahead of the front with north-west (NW) winds and high pressure behind it. The dominant NW and SE trajectories control the measurement area on the day before and after the weather event on 14 May. Therefore a slightly higher pollution level was observed on 13 May than that on 12 May due to the transports of pollutants from the south-east. A clean sky appeared on 15 May due to the transports of clean air mass from north-west. In addition, it should be noted that the heavy rain that happened on 14 May could remove the SO_2, which is highly soluble in water, but not NO_2, which is less soluble, considering that wet deposition could have considerably impacted the pollution conditions. Therefore rainy days (14 May and 4 and 5 June) are not considered in the discussion and in the following analysis about the effects of regional transport.

On 16 May transport of pollutants from the south-west direction can be seen after 14:00 BT. However the concentrations of NO_2 and SO_2 during the transport event on 16 May are much lower than those in the morning of 11 May. The difference might be attributed to the shorter lifetime of NO_2 and SO_2 during daytime than night-time. Therefore we can expect that the gas pollutants, e.g. NO_x, SO_2 and HONO, can be transported to a farther distance during night-time than daytime. Thus night-time regional transport of pollutants from the Wu'an area could significantly pollute the entire measurement area.

In summary we conclude that high pollution levels at the measurement site typically occur if air is transported from the south. Low pollution is associated with other wind directions, especially if air is transported from the north-west briskly behind a cold front. In addition, Y. Wang et al. (2018) demonstrated that particle formations from gas precursors and growths significantly contribute to aerosols and impact the visibility during the campaign. This effect is combined with transports of air mass because activities of particle formations depend on amounts of gas pollutants.

5.2 Systematic analysis of the origin of pollution during the campaign

5.2.1 Source areas of pollutants contributing via regional transport

In order to reveal the effects of transports from different areas on the variations in pollutants observed by MAX-DOAS, we applied a novel procedure based on the backward trajectories. In the procedure, first a grid map of the region around the measurement site within the latitude and longitude ranges of $4°$ (~ 360 km) is created with a spatial resolution of $0.1°$ (~ 10 km). Then we assign the observed column densities of pollutants at the measurement site to individual map pixels, which are connected to the measurement site by backward trajectories. This procedure is performed for individual MAX-DOAS measurements throughout the entire campaign, and all values in the individual pixels are averaged to generate averaged pollution maps. In the reproduced maps, areas with high values of pollution imply that the pollution emissions in the areas could be the dominant source of the high pollution observed at the measurement site via transports. The reproduced maps can be compared with satellite images. The consistencies between the reproduced maps and satellite maps imply that transports could be the dominant source of pollutants and the dominant cause of the day-to-day variations in pollutants observed at the measurement site. The inconsistencies imply that local emissions and local chemical reactions dominate the variability in pollutants. In order to consider pollution transport at different altitudes, we generated individual maps using trajectories ending at 100 m, 300 m, 500 m, 1 km and 2 km above the measurement site. These maps are then averaged to generate the final map. The individual maps using trajectories ending at different altitudes are presented in Fig. S4 in the Supplement. The final maps are shown in Fig. 11. It needs to be noted that similar approaches have been developed and applied to derive regional and global emissions of long-lived atmospheric trace gases and particles (e.g. halocarbons, hydrofluorocarbons, carbon monoxide and black carbon) from in situ measurements, e.g. Stohl et al. (2009), Brunner et al. (2012) and Xu et al. (2013). Emissions of the short-life trace gases are hard to determine using the approach due to variability in their lifetime. Therefore the approach is adapted in the study to only qualitatively analyse effects of pollution transports. The lifetime is only implicitly considered in the approach by using different backward time of trajectories for generating maps.

For NO_2 and SO_2, high values are found in the south-west (near the city of Wu'an), and low values are found in the north-west of the measurement site. For HCHO and AOD, significantly higher values can be seen in the south and east compared to the north-west of the measurement site. The patterns in the created maps are generally consistent with the satellite maps, indicating that air parcels transported from
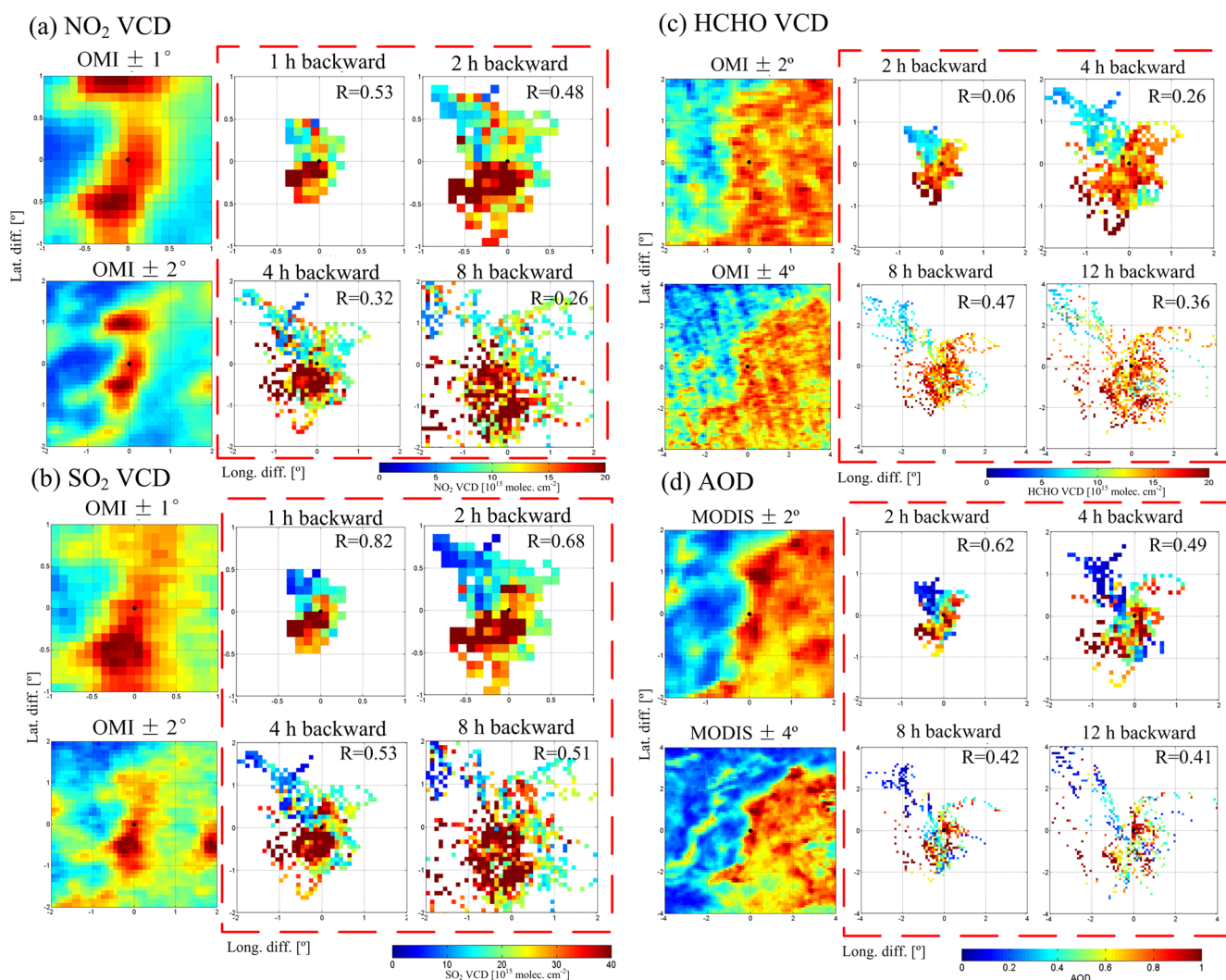
Figure 11. Average reproduced maps (inside the red dashed square) of column densities of NO_2 **(a)**, SO_2 **(b)**, HCHO **(c)** and AOD **(d)** based on MAX-DOAS measurements and back trajectories with different backward times (for details see text), and comparison with maps of the pollutants derived from OMI and MODIS satellite observations. Different times of the backward trajectories are used for the generation of the maps. The correlation coefficients of the pollutants in the reproduced maps against the satellite map are given in individual subfigures. Note that 1° latitude and longitude is about 90 km.

clean or polluted areas considerably contribute to the pollutant levels near the measurement site. Interestingly, the patterns in the reproduced maps change by using different times of the backward trajectories. Correlation coefficients of the values in the reproduced maps against the satellite maps are also shown in Fig. 11 for the maps created for different times of the backward trajectories. Better agreement between the reproduced maps and the satellite maps is found for shorter backward times (1 h) for NO_2, SO_2 and AOD and longer backward times (8 h) for HCHO. This finding is probably related to the typically shorter lifetimes of NO_2 and SO_2 than some VOCs, a source of secondary HCHO. It also indicates that the transport from closer sources is probably more important for NO_2 and SO_2 than the transport from a farther dis-

tance, and vice versa for HCHO. For aerosols the dependence is much weaker than for the trace gases, indicating comparable contributions of short-range and long-range transport to aerosols. In addition, in order to test effects of transport at different altitudes, the resulting maps for different altitudes, shown in Fig. S4 in the Supplement, indicate that pollutants at different altitudes are mainly from the same source directions, but those at higher altitudes could be transported from areas that are farther away.

5.2.2 Characteristics of the pollutants under different dominant trajectories

In order to quantify the differences of pollutants under different dominant transport conditions, we sort the measure-

ment days of the whole campaign into three groups based on the synoptic situation and the dominant directions of the night-time trajectories, including southerly, north-westerly and easterly trajectories. The sorting is also related to synoptic situations. The southerly and north-westerly trajectories are related to the warm sectors ahead of the front and cold sectors behind the front, respectively. The easterly trajectories are for the site controlled by a maritime tropical air mass. Considering that the lifetimes of the observed trace gases are typically longer during night-time than daytime (because of lower OH radical concentrations), the measurement data are sorted mainly based on the night-time trajectories. Nine days (9, 11, 18, 19, 23, 30 and 31 May and 7 and 9 June), 8 days (12, 13, 15, 16, 17, 24, 25 and 26 May) and 8 days (20, 21, 22 and 27 May and 1, 2, 6 and 8 June) fall into these three categories with dominant southerly, north-westerly and easterly trajectories, respectively. Figure S5 in the Supplement presents contributions (percentages) of air mass from different locations in the area ($\pm 2°$ in latitude and $\pm 2°$ in longitude, about $180\,km \times 180\,km$) around the measurement station based on daytime and night-time trajectories for the three groups of days. Figure S5 indicates that most of the trajectories come from the chosen dominant trajectory directions, but a few of them also come from other directions because of the changes of the wind fields during the day. In general, the dominant directions of the daytime trajectories are similar to those of the corresponding night-time trajectories.

Averaged diurnal variations in tropospheric columns and near-surface values of aerosols, NO_2, SO_2, HONO, HCHO and CHOCHO for the three groups of days are shown in Fig. 12 with the corresponding averaged profiles during the morning (06:00–10:00 BT), at around noon (11:00–14:00 BT) and in the afternoon (15:00–18:00 BT). At the bottom of Fig. 12 the averaged diurnal variations in the ratio of HONO to NO_2 (for both VCDs and near-surface VMRs) and the ratio of CHOCHO to HCHO as well as the averaged diurnal variation in the local winds are shown. In order to concisely characterize profile shape, following the procedure in Vlemmix et al. (2015b), the averaged diurnal variations in "characteristic profile heights" H_{75}, which is defined as the height below which 75 % of the integrated profile resides (75 % of the tropospheric column density), is given in Fig. 12. The filters applied to the profile inversion results (see Table 2) could systematically impact results. To avoid drawing a wrong conclusion, the results with and without the filters are shown in Fig. 12: in general the effects of the filters are rather small. The results in Fig. 12 indicate that the values of all gas pollutants are the highest for the southerly trajectories, while the aerosol levels are similar for southerly and easterly trajectories. These findings will be discussed in the following section in more detail. The lowest values (except for NO_2) are found for north-westerly trajectories. These results are consistent with the findings shown in Sect. 5.1 and 5.2.1. Another interesting finding is the exis-

tence of lifted layers of NO_2, SO_2 and aerosols in the morning for the southerly trajectories, indicating the accumulation of pollutants at the top of the boundary layer. This might be caused by the combined effects of higher wind speeds and longer lifetimes at higher altitudes. The averaged H_{75} values are $\sim 1.2\,km$ for NO_2 and SO_2 and $\sim 1.4\,km$ for aerosols, HONO, HCHO and CHOCHO. Systematically lower values of H_{75} for southerly trajectories are found (high pollution) than for north-westerly trajectories (low pollution), especially for NO_2, SO_2 and HONO, of down to $\sim 0.5\,km$ in the morning for southerly trajectories. This phenomenon is related to accumulations of anthropogenic pollutants in the PBL and PBL dynamics.

In order to analyse the influence of local winds, bivariate plots of AOD, and the VCDs of NO_2, SO_2, HONO, HCHO and CHOCHO VCDs as functions of wind speed and directions are shown in Fig. 13 for the three groups of days, respectively. In general the higher values of aerosols, NO_2, SO_2 and HCHO occur for the south-east wind directions than for other wind directions on the days of north-westerly trajectories. This finding possibly indicates the effect of short-range transports of pollutants emitted in the downtown area of Xingtai (with an iron factory) about $20\,km$ south-east of the station. The effect of short-range transport can be identified well when the air mass over the station is dominated by transport of clean air mass from the north-west. But of course, the long-range transport also might have transported the pollutants via the south-east local winds to the measurement site (although in general low pollution levels are found for the north-westerly trajectories; see Fig. 12). The dependences of the pollutants on local winds are not distinct under the two other groups of dominant trajectories. This finding implies two aspects: (1) the Xingtai emissions are not comparable to those from other industrial areas, e.g. near the city of Wu'an, and (2) in the case that regional transport of pollutants from the south leads to large-scale pollution in the measurement area, high values of pollutants can be observed no matter where local winds come from.

Different characteristics are found for the different species in Figs. 12 and 13 and are discussed in the following.

NO_2 and SO_2

Similar patterns of diurnal variations in NO_2 and SO_2 are found in Figs. 12 and 13 and indicate that both species have similar sources and sinks. The increase in NO_2 and SO_2 before 10:00 BT for days with southerly trajectories (Fig. 12b and c) can probably be attributed to the systematic change of westerly local winds (from the mountain area) to south-easterly winds between 06:00 to 10:00 BT (see Fig. 12i). The same effect could cause the observed in high NO_2 and SO_2 values under east-southerly wind conditions with a wind speed smaller than $5\,m\,s^{-1}$ because this wind field frequently occurred around 09:00 BT (see Fig. 12i), when NO_2 and SO_2 levels are high. The decrease in NO_2 and SO_2 after around
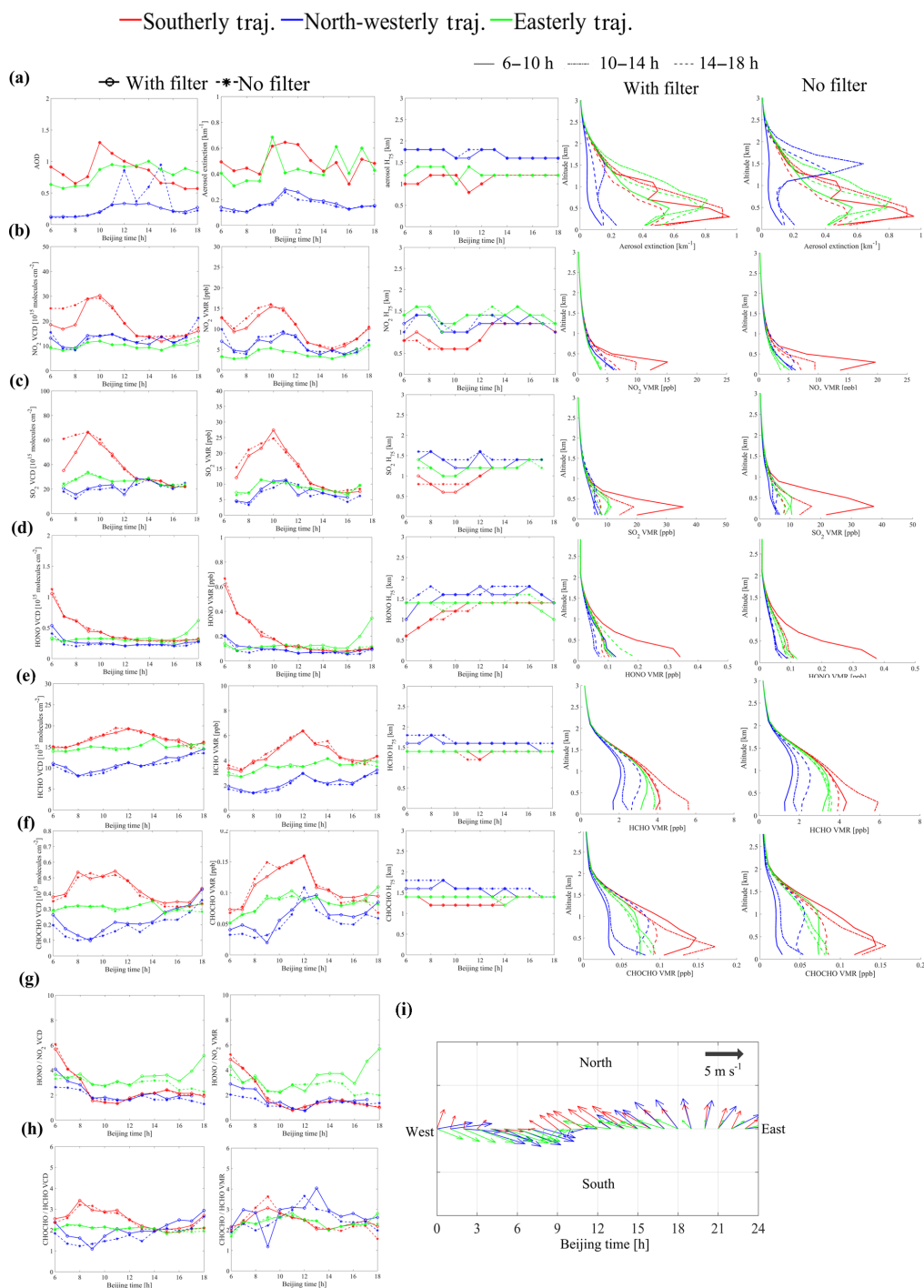
Figure 12. Averaged MAX-DOAS results for the three groups of days with different dominant directions of night-time trajectories (different colours). In the left two columns of panels **(a)** to **(f)**, the diurnal variation in AOD, trace gas VCDs, near-surface aerosol extinction and near-surface trace gas VMRs are shown (circles and stars indicate the filtered and unfiltered results based on the deviations of measured and modelled dSCD in the profile inversion). In the middle column of subfigures, the diurnal variations in H_{75} of retrieved profiles are shown. In the right two columns of subfigures the corresponding averaged profiles for three periods (different line styles) are shown. Panels **(g)**, **(h)** and **(i)** show the averaged ratios of HONO to NO_2 VCD and near-surface VMRs, the averaged ratios of CHOCHO to HCHO VCDs and near-surface VMRs, and the averaged diurnal variation in the local wind fields, respectively. In general, pollutant levels are the highest with winds out of the south and east where major sources reside and lowest with winds out of the north or north-west being generally behind cold fronts. HONO/NO_2 ratios are the highest for winds from the east, where the agricultural activity is, and CHOCHO/HCHO ratios are the highest for back trajectories out of the south, indicating the dominance of petrochemical activity there.
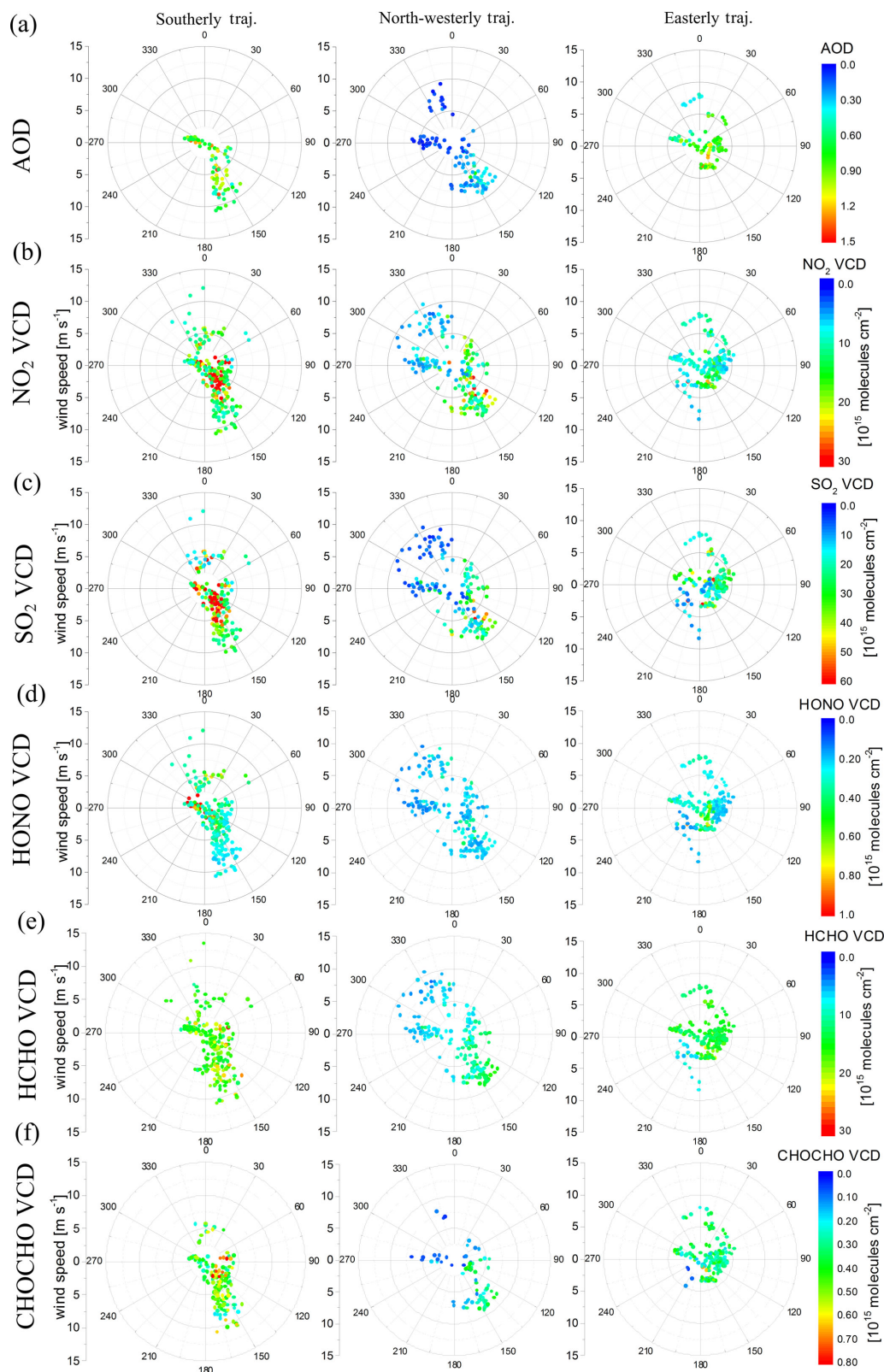
Figure 13. Bivariate figures of AOD **(a)** and VCD of NO$_2$ **(b)**, SO$_2$ **(c)**, HONO **(d)**, HCHO **(e)** and CHOCHO **(f)** as function of wind speed and direction for the three groups of days with the different dominant directions of night-time trajectories. The colours show values of AOD and VCD.

10:00 BT on the days with the southerly and easterly trajectories (Fig. 12b and c) can be probably attributed to photochemical deposition and dispersion. Dispersion is expected to become more effective when the local wind speeds increase in the afternoon (see Fig. 12i).

HONO

For days with dominant southerly trajectories, high values of HONO were observed, especially in the morning (Fig. 12d). These enhancements are consistent with high levels of NO_2 and SO_2, indicating that HONO could have been transported during the night because of the absence of photolysis. Under the southerly trajectories, HONO sharply decreases in the morning and reaches the detection limit of about 0.1 ppb near the surface at around noon due to its fast photolysis. The photolysis-controlled diurnal variations in HONO also impact the plot of the dependence of HONO on local winds (Fig. 13d). There we can see peak values for light westerly winds. This finding can probably be attributed to the systematically dominant westerly wind in the early morning when HONO values are high. The diurnal variations in the ratios of HONO and NO_2 for the three groups of dominant trajectories are also shown in Fig. 12g. Higher HONO/NO_2 ratios of up to 6 % were observed in the early morning, especially for southerly trajectories. This finding is consistent with the results shown in Fig. 5 and could be attributed to the faster deposit of HONO than NO_2. In addition, for the easterly trajectories, HONO values are higher than for the north-westerly trajectories. This finding is due to high daytime HONO values observed between 6 to 8 June, which are sorted into the group of easterly trajectories. The phenomenon is probably related to a special daytime source of HONO.

HCHO and CHOCHO

Significantly higher HCHO and CHOCHO values for southerly trajectories than for the other trajectories are found in Fig. 12e and f, indicating that large proportions of HCHO and CHOCHO sources are related to the transport of anthropogenic emissions from the south-west industrial area. Because of the short lifetime of HCHO and CHOCHO of the order of hours, daytime regional transport of HCHO and CHOCHO are probably not significant, but long-lived VOCs can be expected to be transported and oxidized to HCHO and CHOCHO in the measurement area. In addition, regional transport of HCHO and CHOCHO during night-time could still be possible and explain the high values of HCHO and CHOCHO in the morning. The oxidation of VOCs to HCHO and CHOCHO is probably the dominant source, because the peak values of HCHO and CHOCHO are observed in the late morning and at around noon. Correlation coefficients of the near-surface HCHO and CHOCHO VMR with the O_3 VMR (measured by an in situ O_3 analyser) are about 0.6 at around noon, also indicating a significant contribution of photochemical destruction of VOCs to HCHO and CHOCHO abundances. Moderately high values of HCHO and CHOCHO are found for easterly trajectories, indicating that VOC levels in the eastern area should be considerably higher than in the north-western area. Consistently, the HCHO map derived from the OMI observations in Fig. 2 shows low HCHO values only in the north-western area and comparably high values in all the other areas. Biogenic emissions of VOCs, e.g. isoprene, could also impact the observed HCHO and CHOCHO in May and June. However, the contributions are not comparable to the anthropogenic sources because of the low HCHO and CHOCHO observed for north-westerly trajectories. A large forest area is located in the north-west of the measurement area with a distance of about 30 km. The averaged diurnal variations in the ratio CHOCHO/HCHO in Fig. 12h show larger values for southerly trajectories than for other trajectories, especially in the morning. This could be due to different precursor VOCs and different reaction rates regarding the formation of CHOCHO and HCHO. Higher CHOCHO/HCHO ratios are also observed in a rural area near the city of Guangzhou in southern China (Li et al., 2013). Moreover, burning events of residual farm plants could also have contributed to the observed high HCHO and CHOCHO values for southerly and easterly trajectories. This finding will be discussed in more detail in Sect. 5.3.

Aerosols

Low values of aerosols were observed only for north-westerly trajectories in Fig. 12a. The phenomenon is similar to HCHO and CHOCHO and also consistent with the similar patterns in the satellite maps of AOD and HCHO shown in Fig. 2. Peak values of aerosols at around 10:00 BT for southerly trajectories are probably due to photochemical formations of secondary aerosols and effects of systematic variations in local winds (as for NO_2 and SO_2). The profiles of aerosol extinction shown in Fig. 12a indicate that the lifted layers were frequently observed for southerly and easterly trajectories. The lifted layers could indicate the accumulation and transport of aerosols at high altitudes. In addition burning events of residuals of farm plants could also contribute to aerosols in the measurement area through regional transports. The sources include primary aerosols and secondary aerosols formed in the plume during transports. The effects of burning events will be discussed in more detail in Sect. 5.3.

In general, regional transport, especially during night-time, is the dominant factor which determines the amounts of all pollutants in the measurement area. Local winds and photochemistries play considerable roles in the corresponding diurnal variations. Y. Wang et al. (2018) demonstrated the same conclusion about aerosols regarding the significant effect of regional transport based on aircraft measurements operated in the same campaign region and period.

5.3 Effect of agricultural burning

There are extensive farmlands in the NCP region, and farmers normally burn residuals of plants after harvest, especially wheat straw in May and June. Burning events during the measurement period are identified from the Fire Information for Resource Management System (FIRMS) based on MODIS satellite observations (https://earthdata.nasa.gov/earth-observation-data/near-real-time/citation#ed-firms-citation, last access: 11 April 2019). With the daily total numbers of fire points in the NCP region during the campaign, Fig. 14a shows that frequent burning events occurred on 10, 15, 19, 24 and 29 May and 4 and 9 June. A map of all observed fires during the entire measurement period (Fig. 14b) indicates that burning events mostly appeared in the east and south of the measurement site. Burning impacts air quality on days with southerly and easterly trajectories.

Indeed, high values of HCHO, CHOCHO and aerosols can be seen in Fig. 5 on most days with high numbers of burning events and also 1 or 2 days after the events. In contrast, on 15 and 24 May, when the trajectories originated mainly from north-westerly directions, no enhanced levels of HCHO, CHOCHO and aerosols are found. Therefore we can expect that VOCs and aerosols emitted from the burning plants were transported to the measurement area and considerably impacted the abundances of HCHO, CHOCHO and aerosols (aerosols might also be additionally formed from the photochemical degradation of the VOCs) for southerly and easterly trajectories. VOCs and aerosols emitted from burning events could still impact the measurement area in the 2 days after the events because of their long atmospheric lifetimes. Here it is important to note that although NO_x is probably also emitted from the biomass burning events, it might be mostly destroyed during the transport to the measurement site because of its short lifetime.

One interesting example is found on 6 June for dominant south-easterly trajectories. Peak values of HCHO, CHOCHO, aerosols and ozone are found in the afternoon on 6 June (see Figs. 5 and S3 in the Supplement). However the NO_2 and SO_2 values are quite low. The true colour images of the area observed by MODIS from 4 to 6 June are shown in Fig. 14c, indicating that the whole NCP region is partially cloudy and covered by dense haze with an AOD of up to 2 at 550 nm, but almost no fire points are identified on 6 June. The AOD is derived from the MODIS aerosol product supplied by NASA (http://ladsweb.modaps.eosdis.nasa.gov, last access: 11 April 2019). Many fire points are observed on 4 June, when the aerosol load is low. Although no fire points can be seen on 5 June, this does not necessarily indicate that there are no fires below the clouds because clouds shield satellite observations. Therefore VOCs emitted from the burning events on 4 June (probably also on 5 June) could strongly contribute to the peak values of HCHO, CHOCHO aerosols on 6 June through photochemical reactions. Effective photo-chemical reactions are expected on 6 June due to the cloud-free conditions and are also implied by the high ozone values in the afternoon. Also primary aerosols and secondary nitrate might contribute to the observed high aerosols on 6 June. Consistently, the collocated measurements of the aerosol composition reported in Zhang et al. (2018) demonstrated that the high amounts of aerosols are dominated by organic aerosols (about $40 \, \mu g \, cm^{-3}$ on 6 June) and also have high sulfate and nitrate fractions (about 20 and $15 \, \mu g \, cm^{-3}$). The observed phenomenon of relatively high values of HCHO, CHOCHO and aerosols, but low values of NO_2 and SO_2 for easterly trajectories, could thus at least partly be due to effects of burning events.

5.4 Rough estimates of contributions of regional transports

The local emissions (including the contributions of local transport from the downtown area of city of Xingtai) can be treated as the dominant sources of pollutants for situations with transport from the north-west (the group of days with north-westerly trajectories). The contributions of regional transport to the observed pollutants for the two other groups of days can be roughly estimated based on the relative differences of the pollutant values compared to those for north-westerly trajectories. Tropospheric columns are used for the estimation because regional transport often occurs not directly above the surface. According to this simple calculation, for the days with mainly southerly trajectories, about 47 %, 45 %, 47 %, 34 %, 46 % and 65 % of the observed amounts of NO_2, SO_2, HONO, HCHO, CHOCHO and aerosols can be assigned to the effect of regional transport, respectively. In summary, we find that the total contribution of regional transport to the total amounts of pollutants in the measurement area during the entire measurement period is about 29 %, 25 %, 27 %, 22 %, 28 % and 54 % for NO_2, SO_2, HONO, HCHO, CHOCHO and aerosols, respectively. It needs to be clarified that these results are only rough estimates. The uncertainties largely depend on the uncertainties of the trajectories, variations in the local emissions and chemical reactions. The error budget cannot be constrained well at this stage.

6 Conclusions

Vertical profiles and near-surface and column densities of aerosol extinction, NO_2, SO_2, HONO, HCHO and CHOCHO were retrieved from MAX-DOAS measurements during the period from 8 May to 10 June 2016 at a rural site located on the central western edge of the NCP. The mean value of near-surface aerosol extinction was $\sim 0.43 \, km^{-1}$, with high levels of gaseous pollutants NO_2 (37.8 ppb), SO_2 (17.1 ppb), HONO (0.22 ppb), HCHO (3.3 ppb) and CHOCHO (0.08 ppb). The mean value of AOD at 360 nm was
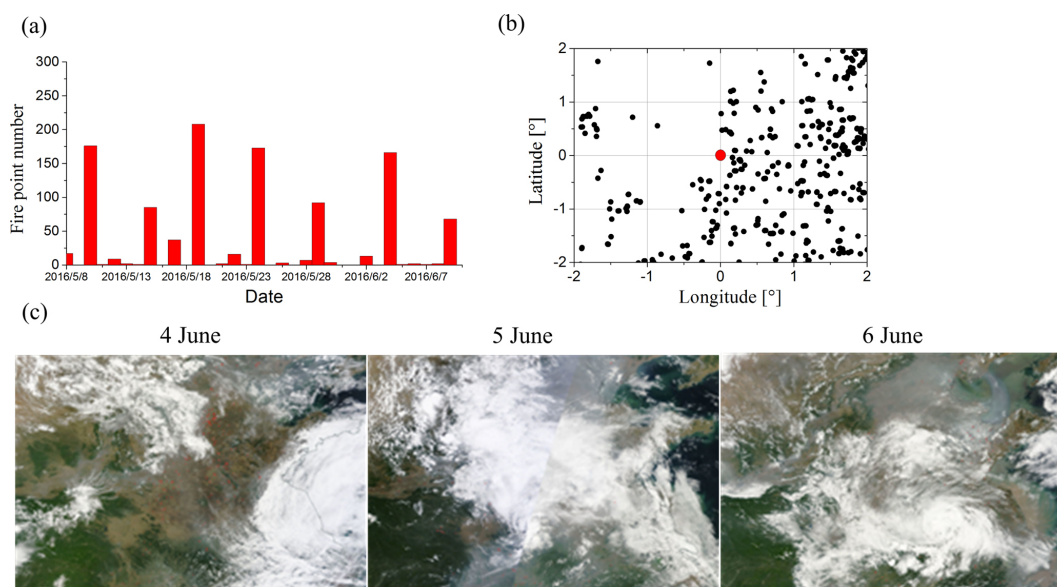
Figure 14. (a) Daily total numbers of fire counts in the NCP region. **(b)** Distributions of fire points in the $2° \times 2°$ (180 km^2) area around the measurement site. **(c)** Images of the NCP region derived from MODIS observations; blue circles and red dots represent the measurement station and fire points, respectively.

~ 0.65, with high VCDs of gaseous pollutants NO_2 (15.6×10^{15} molecules cm^{-2}), SO_2 (31.8×10^{15} molecules cm^{-2}), HONO (0.22×10^{15} molecules cm^{-2}) and HCHO (13.8×10^{15} molecules cm^{-2}). The HONO/NO_2 ratios averaged at 1.9 % to 2.9 % with a peak of about 5 % in the morning on days with transport of air from polluted southern or southwestern areas. CHOCHO/HCHO ratios averaged between 2 % to 2.5 % with a peak of about 3.5 % in the morning on days with transport of air from the polluted areas. Significant day-to-day variations were found for all species mainly due to regional transport of pollutants and changes in synoptic patterns. Agricultural burning events impacted the day-to-day variations in HCHO, CHOCHO and aerosols considerably. Maximum values systematically occurred in the morning for NO_2, SO_2 and HONO but occurred at around noon for aerosols, HCHO and CHOCHO. The diurnal variations were dominated by characteristic photochemistry, upslope–downslope circulation and PBL dynamics. Aerosol, HCHO and CHOCHO profiles with H_{75} of ~ 1.4 km typically extended to higher altitudes than NO_2, SO_2 and HONO with H_{75} as low as 0.5 km under the polluted condition, probably due to secondary formation. Lifted layers were systematically observed for all species (except HONO), indicating accumulation, secondary formation or long-range transport of the pollutants at high altitudes. At high altitudes, pollutants have longer lifetimes and winds are stronger, leading to large-scale adverse impacts.

AOD (R of 0.84, slope of 1.13) and near-surface aerosol extinction (R of 0.81, slope of 1.02) derived from MAX-DOAS measurements were consistent with sun-photometer measurements and visibility-meter measurements under cloud-free conditions with low aerosol loads. Near-surface VMRs of NO_2, SO_2 and HCHO correlated well with in situ measurements with R of 0.9, 0.95 and 0.6, respectively. However, MAX-DOAS results are considerably smaller than the in situ results, mainly due to vertical and horizontal inhomogeneities of trace gases. In general, the agreement of all species between MAX-DOAS and other measurements weakens under cloudy and high aerosol conditions. We further compare profiles of aerosol extinction retrieved from the MAX-DOAS with the lidar measurements on 2 days of simultaneous measurements. Reasonable consistency but also systematic differences are found which were mainly caused by differences in sensitivity as a function of altitude and substantial horizontal gradients of aerosols. Also cloud contamination of MAX-DOAS results is probable for some measurements. Vertical profiles of aerosol extinction, NO_2 and SO_2 VMRs retrieved from MAX-DOAS measurements are also compared with the aircraft measurements on 2 days, and generally indicate reasonable consistency, after the MAX-DOAS averaging kernels are applied to the aircraft data and vertical profiles are extrapolated to observed surface values. The smoothing effect of MAX-DOAS profile retrievals can cause a reshaping of box profiles below 2 km towards exponentially decreasing profiles. This effect can cause MAX-DOAS measurements to significantly underestimate pollutants located at altitudes above 1 km.

We analysed the effects of regional and local transport of pollutants based on case studies and a systematic analysis using the MAX-DOAS measurements, backward trajectories, synoptic situations and local winds. In general, the regional transport, especially during night-time, is found to be the

dominant factor in local air quality. For surface values, local winds, photochemistry and PBL dynamics all exert a strong influence on the diurnal variation in the pollutants. The regional transport of gas pollutants plays a more significant role during night-time than daytime due to longer lifetimes at night. We document regular episodes of regional transport of clean air masses from the north-west (often associated with a cold front) and polluted air masses from the southern industrialized areas around the city of Wu'an with many steel and coal coking facilities. Burning events of crop residuals in the NCP region can considerably impact HCHO, CHOCHO and aerosols. Contributions of regional transport to the total amounts of pollutants in the measurement area during the entire measurement period were 20 % to 30 % for trace gases and about 50 % for aerosols.

Author contributions. YW (affiliation 1) analysed vertical profiles and regional transports of pollutants by combing different data sets and trajectory simulations and prepared the paper with contributions from all co-authors. YW (affiliation 1), StD, SeD and Thomas Wagner designed, operated and analysed the MAX-DOAS measurements. SB contributed to the analysis of regional transports in Sect. 5.2.1. YW (affiliation 4) contributed to the operation of MAX-DOAS measurements. HH, XR and RRD operated and analysed the aircraft measurements. ZD, DLiu, ZW and JX operated and analysed lidar measurements. ZL, DLi and HX operated and analysed sun-photometer measurements. YuW operated in situ measurements. IDS and NT contributed the OMI satellite data of HCHO and SO_2. ZL designed and organized the A^2BC campaign.

References

Aliwell, S. R., Van Roozendael, M., Johnston, P. V., Richter, A., Wagner, T., Arlander, D. W., Burrows, J. P., Fish, D. J., Jones, R. L., Tørnkvist, K. K., Lambert, J.-C., Pfeilsticker, K., and Pundt, I.: Analysis for BrO in zenith-sky spectra: An intercomparison exercise for analysis improvement, J. Geophys. Res., 107, ACH 10-1–ACH 10-20, https://doi.org/10.1029/2001JD000329, 2002.

Anderson, T. L., Covert, D. S., Marshall, S. F., Laucks, M. L., Charlson, R. J., Waggoner, A. P., Ogren, J. A., Caldow, R., Holm, R. L., Quant, F. R., Sem, G. J., Wiedensohler, A., Ahlquist, N. A., and Bates, T. S.: Performance characteristics of a high-sensitivity, three-wavelength, total scatter/backscatter nephelometer, J. Atmos. Ocean. Tech., 13, 967–986, 1996.

Benish, S., He, H., Ren, X., Roberts, S., Li Z., Wang, F., Wang, Y., Zhang F., Shao, M., Lu, S., Pfister, G., Flock, F., and Dickerson, R.: Observations of Nitrogen Oxides and Volatile Organic Compounds over the North China Plain and Impact on Ozone Formation, J. Geophys. Res., in preparation, 2019.

Bobrowski, N., Honninger, G., Galle, B., and Platt, U.: Detection of bromine monoxide in a volcanic plume, Nature, 423, 273–276, 2003.

Boersma, K. F., Eskes, H. J., Veefkind, J. P., Brinksma, E. J., van der A, R. J., Sneep, M., van den Oord, G. H. J., Levelt, P. F., Stammes, P., Gleason, J. F., and Bucsela, E. J.: Near-real time retrieval of tropospheric NO_2 from OMI, Atmos. Chem. Phys., 7, 2103–2118, https://doi.org/10.5194/acp-7-2103-2007, 2007.

Boersma, K. F., Eskes, H. J., Dirksen, R. J., van der A, R. J., Veefkind, J. P., Stammes, P., Huijnen, V., Kleipool, Q. L., Sneep, M., Claas, J., Leitão, J., Richter, A., Zhou, Y., and Brunner, D.: An improved tropospheric NO_2 column retrieval algorithm for the Ozone Monitoring Instrument, Atmos. Meas. Tech., 4, 1905–1928, https://doi.org/10.5194/amt-4-1905-2011, 2011.

Bogumil, K., Orphal, J., Homann, T., Voigt, S., Spietz, P., Fleischmann, O. C., Vogel, A., Hart-mann, M., Kromminga, H., Bovensmann, H., Frerick, J., and Burrows, J. P.: Measurements of molecular absorption spectra with the SCIAMACHY preflight model: instrument characterization and reference data for atmospheric remote-sensing in the 230–2380 nm region, J. Photoch. Photobio. A, 157, 167–184, 2003.

Brent, L. C., Thorn, W. J., Gupta, M., Leen, B., Stehr, J. W., He, H., Arkinson, H. L., Weinheimer, A., Garland, C., Pusede, S. E., Wooldridge, P. J., Cohen, R. C., and Dickerson, R. R.: Evaluation

of the use of a commercially available cavity ringdown absorption spectrometer for measuring NO_2 in flight, and observations over the Mid-Atlantic States, during DISCOVER-AQ, J. Atmos. Chem., 72, 503–521, https://doi.org/10.1007/s10874-013-9265-6, 2013.

Brunner, D., Henne, S., Keller, C. A., Reimann, S., Vollmer, M. K., O'Doherty, S., and Maione, M.: An extended Kalman-filter for regional scale inverse emission estimation, Atmos. Chem. Phys., 12, 3455–3478, https://doi.org/10.5194/acp-12-3455-2012, 2012.

Castellanos, P., Luke, W. T., Kelley, P., Stehr, J. W., Ehrman, S. H., and Dickerson, R. R.: Modification of a commercial cavity ringdown spectroscopy NO_2 detector for enhanced sensitivity, Rev. Sci. Instrum., 80, 113107, https://doi.org/10.1063/1.3244090, 2009.

Chaudhry, Z., Martins, J. V., Li, Z., Tsay, S.-C., Chen, H., Wang, P., Wen, T., Li, C., and Dickerson, R. R.: In situ measurements of aerosol mass concentration and radiative properties in Xianghe, southeast of Beijing, J. Geophys. Res., 112, D23S90, https://doi.org/10.1029/2007JD009055, 2007.

Chen, W. T., Shao, M., Lu, S. H., Wang, M., Zeng, L. M., Yuan, B., and Liu, Y.: Understanding primary and secondary sources of ambient carbonyl compounds in Beijing using the PMF model, Atmos. Chem. Phys., 14, 3047–3062, https://doi.org/10.5194/acp-14-3047-2014, 2014.

Clémer, K., Van Roozendael, M., Fayt, C., Hendrick, F., Hermans, C., Pinardi, G., Spurr, R., Wang, P., and De Mazière, M.: Multiple wavelength retrieval of tropospheric aerosol optical properties from MAXDOAS measurements in Beijing, Atmos. Meas. Tech., 3, 863–878, https://doi.org/10.5194/amt-3-863-2010, 2010.

Danckaert, T., Fayt, C., Van Roozendael, M., De Smedt, I., Letocart, V., Merlaud, A., and Pinardi, G.: QDOAS Software User Manual Version 3.2, Belgian Institute for Space Aeronomy (BIRA-IASB), available at: http://uv-vis.aeronomie.be/software/QDOAS/QDOAS_manual.pdf (last access: 13 April 2019) 2017.

De Smedt, I., Müller, J.-F., Stavrakou, T., van der A, R., Eskes, H., and Van Roozendael, M.: Twelve years of global observations of formaldehyde in the troposphere using GOME and SCIAMACHY sensors, Atmos. Chem. Phys., 8, 4947–4963, https://doi.org/10.5194/acp-8-4947-2008, 2008.

De Smedt, I., Van Roozendael, M., Stavrakou, T., Müller, J.-F., Lerot, C., Theys, N., Valks, P., Hao, N., and van der A, R.: Improved retrieval of global tropospheric formaldehyde columns from GOME-2/MetOp-A addressing noise reduction and instrumental degradation issues, Atmos. Meas. Tech., 5, 2933–2949, https://doi.org/10.5194/amt-5-2933-2012, 2012.

De Smedt, I., Stavrakou, T., Hendrick, F., Danckaert, T., Vlemmix, T., Pinardi, G., Theys, N., Lerot, C., Gielen, C., Vigouroux, C., Hermans, C., Fayt, C., Veefkind, P., Müller, J.-F., and Van Roozendael, M.: Diurnal, seasonal and long-term variations of global formaldehyde columns inferred from combined OMI and GOME-2 observations, Atmos. Chem. Phys., 15, 12519–12545, https://doi.org/10.5194/acp-15-12519-2015, 2015.

Dickerson, R. R., Li, C., Li, Z., Marufu, L. T., Stehr, J. W., McClure, B., Krotkov, N., Chen, H., Wang, P., Xia, X., Ban, X., Gong, F., Yuan, J., and Yang, J.: Aircraft observations of dust and pollutants over northeast China: Insight into the meteorological mechanisms of transport, J. Geophys. Res., 112, D24S90, https://doi.org/10.1029/2007JD008999, 2007.

Ding, A., Wang, T., Xue, L., Gao, J., Stohl, A., Lei, H., Jin, D., Ren, Y., Wang, X., Wei, X., and Qi, Y.: Transport of north China air pollution by midlatitude cyclones: Case study of aircraft measurements in summer 2007, J. Geophys. Res.-Atmos., 114, D08304, https://doi.org/10.1029/2008JD011023, 2009.

Donner, S.: Mobile MAX-DOAS measurements of the tropospheric formaldehyde column in the Rhein – Main Region, Master Thesis, Institute for Atmospheric Physics of the Johannes Gutenberg University Mainz, 2016.

Frieß, U., Monks, P. S., Remedios, J. J., Rozanov, A., Sinreich, R., Wagner, T., and Platt, U.: MAX-DOAS O_4 measurements: A new technique to derive information on atmospheric aerosols: 2. Modeling studies, J. Geophys. Res., 111, D14203, https://doi.org/10.1029/2005JD006618, 2006.

Frieß, U., Sihler, H., and Sander, R.: The vertical distribution of BrO and aerosols in the Arctic: Measurements by active and passive differential optical absorption spectroscopy, J. Geophys. Res., 116, D00R04, https://doi.org/10.1029/2011JD015938, 2011.

Fu, G. Q., Xu, W. Y., Yang, R. F., Li, J. B., and Zhao, C. S.: The distribution and trends of fog and haze in the North China Plain over the past 30 years, Atmos. Chem. Phys., 14, 11949–11958, https://doi.org/10.5194/acp-14-11949-2014, 2014.

Gilpin, T., Apel, E., Fried, A., Wert, B., Calvert, J., Genfa, Z., Dasgupta, P., Harder, J. W., Heikes, B., Hopkins, B., Westberg, H., Kleindienst, T., Lee, Y.-N., Zhou, X., Lonneman, W., and Sewell, S.: Intercomparison of six ambient $[CH_2O]$ measurement techniques, J. Geophys. Res.-Atmos., 102, 21161–21188, 1997.

Han, T., Xu, W., Li, J., Freedman, A., Zhao, J., Wang, Q., Chen, C., Zhang, Y., Wang, Z., Fu, P., Liu, X., and Sun, Y.: Aerosol optical properties measurements by a CAPS single scattering albedo monitor: Comparisons between summer and winter in Beijing, China, J. Geophys. Res.-Atmos., 122, 2513–2526, https://doi.org/10.1002/2016JD025762, 2017.

Hartl, A. and Wenig, M. O.: Regularisation model study for the least-squares retrieval of aerosol extinction time series from UV/VIS MAX-DOAS observations for a ground layer profile parameterisation, Atmos. Meas. Tech., 6, 1959–1980, https://doi.org/10.5194/amt-6-1959-2013, 2013.

He, H., Li, C., Loughner, C. P., Li, Z., Krotkov, N. A., Yang, K., Wang, L., Zheng, Y., Bao, X., Zhao, G., and Dickerson, R. R.: SO_2 over central China: Measurements, numerical simulations and the tropospheric sulfur budget, J. Geophys. Res.-Atmos., 117, D00K37, https://doi.org/10.1029/2011JD016473, 2012.

He, H.: Air pollution concentrations and trends over the Eastern U.S. and China: aircraft measurements and numerical simulations, Dissertation, University of Maryland, College Park, 2012.

He, H., Loughner, C. P., Stehr, J. W., Arkinson, H. L., Brent, L. C., Follette-Cook, M. B., Tzortziou, M. A., Pickering, K. E., Thompson, A. M., Martins, D. K., Diskin, G. S., Anderson, B. E., Crawford, J. H., Weinheimer, A. J., Lee, P., Hains, J. C., and Dickerson, R. R.: An elevated reservoir of air pollutants over the Mid-Atlantic States during the 2011 DISCOVER-AQ campaign: Airborne measurements and numerical simulations, Atmos. Environ., 85, 18–30, 2014.

Hendrick, F., Müller, J.-F., Clémer, K., Wang, P., De Mazière, M., Fayt, C., Gielen, C., Hermans, C., Ma, J. Z., Pinardi, G., Stavrakou, T., Vlemmix, T., and Van Roozendael, M.: Four years of ground-based MAX-DOAS observations of HONO and

NO$_2$ in the Beijing area, Atmos. Chem. Phys., 14, 765–781, https://doi.org/10.5194/acp-14-765-2014, 2014.

Henyey, L. G. and Greenstein, J. L.: Diffuse radiation in the galaxy, Astrophys. J., 93, 70–83, 1941.

Hönninger, G. and Platt, U.: Observations of BrO and its vertical distribution during surface ozone depletion at Alert, Atmos. Environ., 36, 2481–2489, 2002.

Hönninger, G., von Friedeburg, C., and Platt, U.: Multi axis differential optical absorption spectroscopy (MAX-DOAS), Atmos. Chem. Phys., 4, 231–254, https://doi.org/10.5194/acp-4-231-2004, 2004.

Huang, R.-J., Zhang, Y., Bozzetti, C., Ho, K.-F., Cao, J., Han, Y., Dällenbach, K. R., Slowik, J. G., Platt, S. M., Canonaco, F., Zotter, P., Wolf, R., Pieber, S. M., Bruns, E. A., Crippa, M., Ciarelli, G., Piazzalunga, A., Schwikowski, M., Abbaszade, G., Schnelle-Kreis, J., Zimmermann, R., An, Z., Szidat, S., Baltensperger, U., Haddad, I. E., and Prévôt, A. S. H.: High secondary aerosol contribution to particulate pollution during haze events in China, Nature, 514, 218–222, 2014.

Irie, H., Kanaya, Y., Akimoto, H., Iwabuchi, H., Shimizu, A., and Aoki, K.: First retrieval of tropospheric aerosol profiles using MAX-DOAS and comparison with lidar and sky radiometer measurements, Atmos. Chem. Phys., 8, 341–350, https://doi.org/10.5194/acp-8-341-2008, 2008.

Irie, H., Takashima, H., Kanaya, Y., Boersma, K. F., Gast, L., Wittrock, F., Brunner, D., Zhou, Y., and Van Roozendael, M.: Eight-component retrievals from ground-based MAX-DOAS observations, Atmos. Meas. Tech., 4, 1027–1044, https://doi.org/10.5194/amt-4-1027-2011, 2011.

Jin, J., Ma, J., Lin, W., Zhao, H., Shaiganfar, R., Beirle, S., and Wagner, T.: MAX-DOAS measurements and satellite validation of tropospheric NO$_2$ and SO$_2$ vertical column densities at a rural site of North China, Atmos. Environ., 133, 12–25, https://doi.org/10.1016/j.atmosenv.2016.03.031, 2016.

Kanaya, Y., Irie, H., Takashima, H., Iwabuchi, H., Akimoto, H., Sudo, K., Gu, M., Chong, J., Kim, Y. J., Lee, H., Li, A., Si, F., Xu, J., Xie, P.-H., Liu, W.-Q., Dzhola, A., Postylyakov, O., Ivanov, V., Grechko, E., Terpugova, S., and Panchenko, M.: Long-term MAX-DOAS network observations of NO$_2$ in Russia and Asia (MADRAS) during the period 2007–2012: instrumentation, elucidation of climatology, and comparisons with OMI satellite observations and global model simulations, Atmos. Chem. Phys., 14, 7909–7927, https://doi.org/10.5194/acp-14-7909-2014, 2014.

Kaufman, Y. J., Tanré, D., and Boucher, O.: A satellite view of aerosols in the climate system, Nature, 419, 215–223, 2002.

Kraus, S.: DOASIS, A Framework Design for DOAS, PhD thesis, University of Mannheim, Germany, 2006.

Krotkov, N. A., McClure, B., Dickerson, R. R., Carn, S. A., Li, C., Bhartia, P. K., Yang, K., Krueger, A. J., Li, Z., Levelt, P. F., and Chen, H.: Validation of SO$_2$ retrievals from the Ozone Monitoring Instrument over NE China, J. Geophys. Res.-Atmos., 113, D16S40, https://doi.org/10.1029/2007JD008818, 2008.

Lee, Y. N., Zhou, X., Kleinman, L. I., Nunnermacker, L. J., Springston, S. R., Daum, P. H., Newman, L., Keigley, W. G., Holdren, M. W., Spicer, C. W., Young, V., Fu, B., Parrish, D. D., Holloway, J., Williams, J., Roberts, J. M., Ryerson, T. B., and Fehsenfeld, F. C.: Atmospheric chemistry and distribution of formaldehyde and several multioxygenated carbonyl compounds during the 1995 Nashville/Middle Tennessee Ozone Study, J. Geophys. Res., 103, 22449–22462, https://doi.org/10.1029/98jd01251, 1998.

Lei, W., Zavala, M., de Foy, B., Volkamer, R., Molina, M. J., and Molina, L. T.: Impact of primary formaldehyde on air pollution in the Mexico City Metropolitan Area, Atmos. Chem. Phys., 9, 2607–2618, https://doi.org/10.5194/acp-9-2607-2009, 2009.

Levelt, P. F., Hilsenrath, E., Lepppelmeier, G. W., van den Oord, G. H. J., Bhartia, P. K., Taminnen, J., de Haan, J. F., and Veefkind, J. P.: Science objectives of the Ozone Monitoring Instrument, IEEE T. Geosci. Remote Sens., 44, 1199–1208, 2006a.

Levelt, P. F., van den Oord, G. H. J., Dobber, M. R., Malkki, A., Visser, H., de Vries, J., Stammes, P., Lundell, J., and Saari, H.: The Ozone Monitoring Instrument, IEEE T. Geosci. Remote Sens., 44, 1093–1101, 2006b.

Li, C., Marufu, L. T., Dickerson, R. R., Li, Z., Wen, T., Wang, Y., Wang, P., Chen, H., and Stehr, J. W.: In situ measurements of trace gases and aerosol optical properties at a rural site in northern China during East Asian Study of Tropospheric Aerosols: An International Regional Experiment 2005, J. Geophys. Res.-Atmos., 112, D22S04, https://doi.org/10.1029/2006JD007592, 2007.

Li, C., Krotkov, N. A., Dickerson, R. R., Li, Z., Yang, K., and Chin, M.: Transport and evolution of a pollution plume from northern China: A satellite-based case study, J. Geophys. Res., 115, D00K03, https://doi.org/10.1029/2009JD012245, 2010.

Li, C., McLinden, C., Fioletov, V., Krotkov, N., Carn, S., Joiner, J., Streets, D., He, H., Ren, X., Li, Z., and Dickerson, R. R.: India is overtaking China as the world's largest emitter of anthropogenic sulfur dioxide, Sci. Rep.-UK, 7, 14304, https://doi.org/10.1038/s41598-017-14639-8, 2017.

Li, J., Liu, X., Yuan, L., Yin, Y., Li, Z., Li, P., Ren, G., Jin, L., Li, R., and Dong, Z.: Vertical distribution of aerosol optical properties based on aircraft measurements over the Loess Plateau in China, J. Environ. Sci., 34, 44–56, 2015.

Li, X., Brauers, T., Shao, M., Garland, R. M., Wagner, T., Deutschmann, T., and Wahner, A.: MAX-DOAS measurements in southern China: retrieval of aerosol extinctions and validation using ground-based in-situ data, Atmos. Chem. Phys., 10, 2079–2089, https://doi.org/10.5194/acp-10-2079-2010, 2010.

Li, X., Brauers, T., Häseler, R., Bohn, B., Fuchs, H., Hofzumahaus, A., Holland, F., Lou, S., Lu, K. D., Rohrer, F., Hu, M., Zeng, L. M., Zhang, Y. H., Garland, R. M., Su, H., Nowak, A., Wiedensohler, A., Takegawa, N., Shao, M., and Wahner, A.: Exploring the atmospheric chemistry of nitrous acid (HONO) at a rural site in Southern China, Atmos. Chem. Phys., 12, 1497–1513, https://doi.org/10.5194/acp-12-1497-2012, 2012.

Li, X., Brauers, T., Hofzumahaus, A., Lu, K., Li, Y. P., Shao, M., Wagner, T., and Wahner, A.: MAX-DOAS measurements of NO$_2$, HCHO and CHOCHO at a rural site in Southern China, Atmos. Chem. Phys., 13, 2133–2151, https://doi.org/10.5194/acp-13-2133-2013, 2013.

Li, X., Rohrer, F., Hofzumahaus, A., Brauers, T., Häseler, R., Bohn, B., Broch, S., Fuchs, H., Gomm, S., Holland, F., and Jäger, J.: Missing gas-phase source of HONO inferred from Zeppelin measurements in the troposphere, Science, 344, 292–296, https://doi.org/10.1126/science.1248999, 2014.

Li, Z. Q., Xia, X., Cribb, M., Mi, W., Holben, B., Wang, P., Chen, H., Tsay, S. C., Eck, T. F., Zhao, F., and Dutton,

E. G.: Aerosol optical properties and their radiative effects in northern China, J. Geophys. Res.-Atmos., 112, D22S01, https://doi.org/10.1029/2006JD007382, 2007a.

Li, Z. Q., Chen, H., Cribb, M., Dickerson, R., Holben, B., Li, C., Lu, D., Luo, Y., Maring, H., Shi, G., Tsay, S.-C., Wang, P., Wang, Y., Xia, X., Zheng, Y., Yuan, T., and Zhao, F.: Preface to special section: Overview of the East Asain Study of Tropospheric Aerosols: an International Regional Experiment (EAST-AIRE), J. Geophys. Res., 112, D22S00, https://doi.org/10.1029/2007JD008853, 2007b.

Liu, D., Tao, Z., Wu, D., Wang, Z., Wang, B. X., Zhong, Z. Q., Bo, G. Y., Xie, C., Zhou, J., and Wang, Y.: Development of Three-Wavelength Raman Polarization Lidar System and Case Study, Acta Optica Sinica, 33, 0228001, https://doi.org/10.3788/AOS201333.0228001, 2013.

Luke, W. T.: Evaluation of a commercial pulsed fluorescence detector for the measurement of low-level SO_2 concentrations during the gas-phase sulfur intercomparison experiment, J. Geophys. Res.-Atmos., 102, 16255–16265, 1997.

Ma, J. Z., Wang, W., Chen, Y., Liu, H. J., Yan, P., Ding, G. A., Wang, M. L., Sun, J., and Lelieveld, J.: The IPAC-NC field campaign: a pollution and oxidization pool in the lower atmosphere over Huabei, China, Atmos. Chem. Phys., 12, 3883–3908, https://doi.org/10.5194/acp-12-3883-2012, 2012.

Ma, J. Z., Beirle, S., Jin, J. L., Shaiganfar, R., Yan, P., and Wagner, T.: Tropospheric NO2 vertical column densities over Beijing: results of the first three years of ground-based MAX-DOAS measurements (2008–2011) and satellite validation, Atmos. Chem. Phys., 13, 1547–1567, https://doi.org/10.5194/acp-13-1547-2013, 2013.

Marquard, L. C., Wagner, T., and Platt, U.: Improved air mass factor concepts for scattered radiation differential optical absorption spectroscopy of atmospheric species, J. Geophys. Res., 105, 1315–1327, https://doi.org/10.1029/1999JD900340, 2000.

Meller, R. and Moortgat, G. K.: Temperature dependence of the absorption cross sections of formaldehyde between 223 and 323 K in the wavelength range 225–375 nm, J. Geophys. Res., 105, 7089–7101, 2000

MEP: 2016 Report on the State of the Environment in China, MEP, Beijing, China, available at: http://english.mee.gov.cn/Resources/Reports/soe/ReportSOE/201709/P020170929573904364594.pdf (last access: 13 April 2019), 2017 (in Chinese).

Miao, Y., Hu, X. M., Liu, S., Qian, T., Xue, M., Zheng, Y., and Wang, S.: Seasonal variation of local atmospheric circulations and boundary layer structure in the Beijing-Tianjin-Hebei region and implications for air quality, J. Adv. Model. Earth Sy., 7, 1602–1626, 2015.

Ortega, I., Koenig, T., Sinreich, R., Thomson, D., and Volkamer, R.: The CU 2-D-MAX-DOAS instrument – Part 1: Retrieval of 3-D distributions of NO2 and azimuth-dependent OVOC ratios, Atmos. Meas. Tech., 8, 2371–2395, https://doi.org/10.5194/amt-8-2371-2015, 2015.

Pagsberg, P., Bjergbakke, E., Ratajczak, E., and Sillesen, A.: Kinetics of the gas phase reaction $OH + NO (+M) - > O (+M)$ and the determination of the UV absorption cross sections of HONO, Chem. Phys. Lett., 272, 383–390, https://doi.org/10.1016/S0009-2614(97)00576-9, 1997.

Platt, U. and Stutz, J.: Differential Optical Absorption Spectroscopy, Springer, Heidelberg, Berlin, 229–375, 2008.

Polyansky, O. L., Kyuberis, A. A., Zobov, N. F., Tennyson, J., Yurchenko, S. N., and Lodi, L.: ExoMol molecular line lists XXX: a complete high-accuracy line list for water, Mon. Not. R. Astron. Soc., 480, 2597–2608, 2018

Pukīte, J., Kühl, S., Deutschmann, T., Platt, U., and Wagner, T.: Extending differential optical absorption spectroscopy for limb measurements in the UV, Atmos. Meas. Tech., 3, 631–653, https://doi.org/10.5194/amt-3-631-2010, 2010.

Rappenglück, B., Dasgupta, P. K., Leuchner, M., Li, Q., and Luke, W.: Formaldehyde and its relation to CO, PAN, and SO_2 in the Houston-Galveston airshed, Atmos. Chem. Phys., 10, 2413–2424, https://doi.org/10.5194/acp-10-2413-2010, 2010.

Rodgers, C. D.: Inverse methods for atmospheric sounding, theory and practice, Series on Atmospheric, Oceanic and Planetary Physics, World Scientific, Singapore, 2000.

Roscoe, H. K., Van Roozendael, M., Fayt, C., du Piesanie, A., Abuhassan, N., Adams, C., Akrami, M., Cede, A., Chong, J., Clémer, K., Friess, U., Gil Ojeda, M., Goutail, F., Graves, R., Griesfeller, A., Grossmann, K., Hemerijckx, G., Hendrick, F., Herman, J., Hermans, C., Irie, H., Johnston, P. V., Kanaya, Y., Kreher, K., Leigh, R., Merlaud, A., Mount, G. H., Navarro, M., Oetjen, H., Pazmino, A., Perez-Camacho, M., Peters, E., Pinardi, G., Puentedura, O., Richter, A., Schönhardt, A., Shaiganfar, R., Spinei, E., Strong, K., Takashima, H., Vlemmix, T., Vrekoussis, M., Wagner, T., Wittrock, F., Yela, M., Yilmaz, S., Boersma, F., Hains, J., Kroon, M., Piters, A., and Kim, Y. J.: Intercomparison of slant column measurements of NO2 and O4 by MAX-DOAS and zenith-sky UV and visible spectrometers, Atmos. Meas. Tech., 3, 1629–1646, https://doi.org/10.5194/amt-3-1629-2010, 2010.

Rozanov, A., Rozanov, V., Buchwitz, M., Kokhanovsky, A., and Burrows, J.: SCIATRAN 2.0 – A new radiative transfer model for geophysical applications in the 175–2400 nm spectral region, Adv. Space Res., 36, 1015–1019, https://doi.org/10.1016/j.asr.2005.03.012, 2005.

Schreier, S. F., Peters, E., Richter, A., Lampel, J., Wittrock, F., and Burrows, J. P.: Ship-based MAX-DOAS measurements of tropospheric NO2 and SO2 in the South China and Sulu Sea, Atmos. Environ., 102, 331–343, 2015.

Sörgel, M., Trebs, I., Serafimovich, A., Moravek, A., Held, A., and Zetzsch, C.: Simultaneous HONO measurements in and above a forest canopy: influence of turbulent exchange on mixing ratio differences, Atmos. Chem. Phys., 11, 841–855, https://doi.org/10.5194/acp-11-841-2011, 2011a.

Stein, A. F., Draxler, R. R., Rolph, G. D., Stunder, B. J., Cohen, M. D., and Ngan, F.: NOAA's HYSPLIT atmospheric transport and dispersion modeling system, B. Am. Meteorol. Soc., 96, 2059–2077, 2015.

Stohl, A., Seibert, P., Arduini, J., Eckhardt, S., Fraser, P., Greally, B. R., Lunder, C., Maione, M., Mühle, J., O'Doherty, S., Prinn, R. G., Reimann, S., Saito, T., Schmidbauer, N., Simmonds, P. G., Vollmer, M. K., Weiss, R. F., and Yokouchi, Y.: An analytical inversion method for determining regional and global emissions of greenhouse gases: Sensitivity studies and application to halocarbons, Atmos. Chem. Phys., 9, 1597–1620, https://doi.org/10.5194/acp-9-1597-2009, 2009.

Stuhl, F. and Niki, H.: Flash photochemical study of the reaction OH + NO + M using resonance fluorescent detection of OH, J. Chem. Phys., 57, 3677–3679, https://doi.org/10.1063/1.1678826, 1972.

Stutz, J., Kim, E. S., Platt, U., Bruno, P., Perrino, C., and Febo, A.: UV-vis Absorption Cross-Section of Nitrous Acid, J. Geophys. Res., 105, 14585–14592, 2000.

Su, H., Cheng, Y. F., Shao, M., Gao, D. F., Yu, Z. Y., Zeng, L. M., Slanina, J., Zhang, Y. H., and Wiedensohler, A.: Nitrous acid (HONO) and its daytime sources at a rural site during the 2004 PRIDE-PRD experiment in China, J. Geophys. Res.-Atmos., 113, D14312, https://doi.org/10.1029/2007JD009060, 2008.

Su, H., Cheng, Y., Oswald, R., Behrendt, T., Trebs, I., Meixner, F. X., Andreae, M. O., Cheng, P., Zhang, Y., and Pöschl, U.: Soil nitrite as a source of atmospheric HONO and OH radicals, Science, 333, 1616–1618, https://doi.org/10.1126/science.1207687, 2011.

Tao, M., Chen, L., Su, L., and Tao, J.: Satellite observation of regional haze pollution over the North China Plain, J. Geophys. Res.-Atmos., 117, D12203, https://doi.org/10.1029/2012JD017915, 2012.

Tao, Z., Liu, D., Zhong, Z., Shi, B., Nie, M., Ma, X., and Zhou, J.: Measurements of cirrus clouds with a three-wavelength lidar, Chin. Opt. Lett., 10, 050101, 2012.

Taubman, B. F., Hains, J. C., Thompson, A. M., Marufu, L. T., Doddridge, B. G., Stehr, J. W., Piety, C. A., and Dickerson, R. R.: Aircraft vertical profiles of trace gas and aerosol pollution over the Mid-Atlantic United States: Statistics and meteorological cluster analysis, J. Geophys. Res.-Atmos., 111, D10s07, https://doi.org/10.1029/2005jd006196, 2006.

Thalman, R. M. and Volkamer, R.: Temperature Dependent Absorption Cross-Sections of O_2-$O-2$ collision pairs between 340 and 630 nm and at atmospherically relevant pressure, Phys. Chem. Chem. Phys., 15, 15371–15381, https://doi.org/10.1039/c3cp50968k, 2013

Theys, N., De Smedt, I., Gent, J., Danckaert, T., Wang, T., Hendrick, F., Stavrakou, T., Bauduin, S., Clarisse, L., Li, C., Krotkov, N., Yu, H., Brenot, H., and Van Roozendael, M.: Sulfur dioxide vertical column DOAS retrievals from the Ozone Monitoring Instrument: Global observations and comparison to ground/based and satellite data, J. Geophys. Res.-Atmos., 120, 2470–2491, 2015.

Vandaele, A. C., Hermans, C., Simon, P. C., Carleer, M., Colin, R., Fally, S., Mérienne, M.-F., Jenouvrier, A., and Coquart, B.: Measurements of the NO_2 absorption cross section from $42\,000\,cm^{-1}$ to $10000\,cm^{-1}$ (238–1000 nm) at 220 K and 294 K, J. Quant. Spectrosc. Ra., 59, 171–184, 1998.

Van Roozendael, M., Fayt, C., Post, P., Hermans, C., and Lambert, J.-C.: Retrieval of BrO and NO_2 from UV-Visible Observations, in: Sounding the troposphere from space: a new Era for Atmospheric Chemistry. The TROPOSAT Final Report, edited by: Borrell, P., Borrell, P. M., Burrows, J. P., and Platt, U., Springer, New York, 155–166, 2003.

Vlemmix, T., Piters, A. J. M., Stammes, P., Wang, P., and Levelt, P. F.: Retrieval of tropospheric NO_2 using the MAX-DOAS method combined with relative intensity measurements for aerosol correction, Atmos. Meas. Tech., 3, 1287–1305, https://doi.org/10.5194/amt-3-1287-2010, 2010.

Vlemmix, T., Piters, A. J. M., Berkhout, A. J. C., Gast, L. F. L., Wang, P., and Levelt, P. F.: Ability of the MAX-DOAS method to derive profile information for NO_2: can the boundary layer and free troposphere be separated?, Atmos. Meas. Tech., 4, 2659–2684, https://doi.org/10.5194/amt-4-2659-2011, 2011.

Vlemmix, T., Eskes, H. J., Piters, A. J. M., Schaap, M., Sauter, F. J., Kelder, H., and Levelt, P. F.: MAX-DOAS tropospheric nitrogen dioxide column measurements compared with the Lotos-Euros air quality model, Atmos. Chem. Phys., 15, 1313–1330, https://doi.org/10.5194/acp-15-1313-2015, 2015a.

Vlemmix, T., Hendrick, F., Pinardi, G., De Smedt, I., Fayt, C., Hermans, C., Piters, A., Wang, P., Levelt, P., and Van Roozendael, M.: MAX-DOAS observations of aerosols, formaldehyde and nitrogen dioxide in the Beijing area: comparison of two profile retrieval approaches, Atmos. Meas. Tech., 8, 941–963, https://doi.org/10.5194/amt-8-941-2015, 2015b.

Vrekoussis, M., Wittrock, F., Richter, A., and Burrows, J. P.: GOME-2 observations of oxygenated VOCs: what can we learn from the ratio glyoxal to formaldehyde on a global scale?, Atmos. Chem. Phys., 10, 10145–10160, https://doi.org/10.5194/acp-10-10145-2010, 2010.

Wagner, T., Dix, B., von Friedeburg, C., Frieß, U., Sanghavi, S., Sinreich, R., and Platt, U.: MAX-DOAS O_4 measurements: A new technique to derive information on atmospheric aerosols – Principles and information content, J. Geophys. Res., 109, D22205, https://doi.org/10.1029/2004JD004904, 2004.

Wagner, T., Beirle, S., and Deutschmann, T.: Three-dimensional simulation of the Ring effect in observations of scattered sun light using Monte Carlo radiative transfer models, Atmos. Meas. Tech., 2, 113–124, https://doi.org/10.5194/amt-2-113-2009, 2009.

Wagner, T., Beirle, S., Brauers, T., Deutschmann, T., Frieß, U., Hak, C., Halla, J. D., Heue, K. P., Junkermann, W., Li, X., Platt, U., and Pundt-Gruber, I.: Inversion of tropospheric profiles of aerosol extinction and HCHO and NO_2 mixing ratios from MAX-DOAS observations in Milano during the summer of 2003 and comparison with independent data sets, Atmos. Meas. Tech., 4, 2685–2715, https://doi.org/10.5194/amt-4-2685-2011, 2011.

Wagner, T., Apituley, A., Beirle, S., Dörner, S., Friess, U., Remmers, J., and Shaiganfar, R.: Cloud detection and classification based on MAX-DOAS observations, Atmos. Meas. Tech., 7, 1289–1320, https://doi.org/10.5194/amt-7-1289-2014, 2014.

Wagner, T., Beirle, S., Remmers, J., Shaiganfar, R., and Wang, Y.: Absolute calibration of the colour index and O_4 absorption derived from Multi AXis (MAX-)DOAS measurements and their application to a standardised cloud classification algorithm, Atmos. Meas. Tech., 9, 4803–4823, https://doi.org/10.5194/amt-9-4803-2016, 2016.

Wang, F., Li, Z., Ren, X., Jiang, Q., He, H., Dickerson, R. R., Dong, X., and Lv, F.: Vertical distributions of aerosol optical properties during the spring 2016 ARIAs airborne campaign in the North China Plain, Atmos. Chem. Phys., 18, 8995–9010, https://doi.org/10.5194/acp-18-8995-2018, 2018.

Wang, L., Xu, J., Yang, J., Zhao, X., Wei, W., Cheng, D., Pan, X., and Su, J.: Understanding haze pollution over the southern Hebei area of China using the CMAQ model, Atmos. Environ., 56, 69–79, 2012.

Wang, L., Wei, Z., Wei, W., Fu, J. S., Meng, C., and Ma, S.: Source apportionment of $PM_{2.5}$ in top polluted cities in Hebei, China using the CMAQ model, Atmos. Environ., 122, 723–736, 2015.

Wang, T., Hendrick, F., Wang, P., Tang, G., Clémer, K., Yu, H., Fayt, C., Hermans, C., Gielen, C., Müller, J.-F., Pinardi, G., Theys, N., Brenot, H., and Van Roozendael, M.: Evaluation of tropospheric SO_2 retrieved from MAX-DOAS measurements in Xianghe, China, Atmos. Chem. Phys., 14, 11149–11164, https://doi.org/10.5194/acp-14-11149-2014, 2014.

Wang, Y., Li, A., Xie, P. H., Chen, H., Xu, J., Wu, F. C., Liu, J. G., and Liu, W. Q.: Retrieving vertical profile of aerosol extinction by multi-axis differential optical absorption spectroscopy, Acta Phys. Sin.-Ch. Ed., 16, 180705, https://doi.org/10.7498/aps.62.180705, 2013a.

Wang, Y., Li, A., Xie, P. H., Chen, H., Mou, F. S., Xu, J., Wu, F. C., Zeng, Y., Liu, J. G., and Liu, W. Q.: Measuring tropospheric vertical distribution and vertical column density of NO_2 by multi-axis differential optical absorption spectroscopy, Acta Phys. Sin.-Ch. Ed., 16, 200705, https://doi.org/10.7498/aps.62.200705, 2013b.

Wang, Y., Penning de Vries, M., Xie, P. H., Beirle, S., Dörner, S., Remmers, J., Li, A., and Wagner, T.: Cloud and aerosol classification for 2.5 years of MAX-DOAS observations in Wuxi (China) and comparison to independent data sets, Atmos. Meas. Tech., 8, 5133–5156, https://doi.org/10.5194/amt-8-5133-2015, 2015.

Wang, Y., Lampel, J., Xie, P., Beirle, S., Li, A., Wu, D., and Wagner, T.: Ground-based MAX-DOAS observations of tropospheric aerosols, NO_2, SO_2 and HCHO in Wuxi, China, from 2011 to 2014, Atmos. Chem. Phys., 17, 2189–2215, https://doi.org/10.5194/acp-17-2189-2017, 2017a.

Wang, Y., Beirle, S., Lampel, J., Koukouli, M., De Smedt, I., Theys, N., Li, A., Wu, D., Xie, P., Liu, C., Van Roozendael, M., Stavrakou, T., Müller, J.-F., and Wagner, T.: Validation of OMI, GOME-2A and GOME-2B tropospheric NO_2, SO_2 and HCHO products using MAX-DOAS observations from 2011 to 2014 in Wuxi, China: investigation of the effects of priori profiles and aerosols on the satellite products, Atmos. Chem. Phys., 17, 5007–5033, https://doi.org/10.5194/acp-17-5007-2017, 2017b.

Wang, Y., Beirle, S., Hendrick, F., Hilboll, A., Jin, J., Kyuberis, A. A., Lampel, J., Li, A., Luo, Y., Lodi, L., Ma, J., Navarro, M., Ortega, I., Peters, E., Polyansky, O. L., Remmers, J., Richter, A., Puentedura, O., Van Roozendael, M., Seyler, A., Tennyson, J., Volkamer, R., Xie, P., Zobov, N. F., and Wagner, T.: MAX-DOAS measurements of HONO slant column densities during the MAD-CAT campaign: inter-comparison, sensitivity studies on spectral analysis settings, and error budget, Atmos. Meas. Tech., 10, 3719–3742, https://doi.org/10.5194/amt-10-3719-2017, 2017c.

Wang, Y., Li, Z., Zhang, Y., Du, W., Zhang, F., Tan, H., Xu, H., Fan, T., Jin, X., Fan, X., Dong, Z., Wang, Q., and Sun, Y.: Characterization of aerosol hygroscopicity, mixing state, and CCN activity at a suburban site in the central North China Plain, Atmos. Chem. Phys., 18, 11739–11752, https://doi.org/10.5194/acp-18-11739-2018, 2018.

Wei, W. X., Zhang, X., and Tian, G. Q.: Analysis of relation between haze distribution and terrain and wind speed in Hebei Province, Journal of Natural Disasters, 19, 49–52, 2010.

Wittrock, F.: The Retrieval of Oxygenated Volatile Organic Compounds by Remote Sensing Techniques, PhD, University of Bremen, Bremen, Germany, available at: http://www.doas-bremen.de/paper/diss_wittrock_06.pdf (last access: December 2015), 2006.

Wittrock, F., Oetjen, H., Richter, A., Fietkau, S., Medeke, T., Rozanov, A., and Burrows, J. P.: MAX-DOAS measurements of atmospheric trace gases in Ny-Ålesund – Radiative transfer studies and their application, Atmos. Chem. Phys., 4, 955–966, https://doi.org/10.5194/acp-4-955-2004, 2004.

Wojtal, P., Halla, J. D., and McLaren, R.: Pseudo steady states of HONO measured in the nocturnal marine boundary layer: a conceptual model for HONO formation on aqueous surfaces, Atmos. Chem. Phys., 11, 3243–3261, https://doi.org/10.5194/acp-11-3243-2011, 2011.

Xu, W. Y., Zhao, C. S., Ran, L., Deng, Z. Z., Ma, N., Liu, P. F., Lin, W. L., Yan, P., and Xu, X. B.: A new approach to estimate pollutant emissions based on trajectory modeling and its application in the North China Plain, Atmos. Environ., 71, 75–83, 2013.

Yilmaz, S.: Retrieval of Atmospheric Aerosol and Trace Gas Vertical Profiles using Multi-Axis Differential Optical Absorption Spectroscopy, PhD thesis, University of Heidelberg, Germany, 2012.

Yu, Y., Galle, B., Panday, A., Hodson, E., Prinn, R., and Wang, S.: Observations of high rates of NO_2-HONO conversion in the nocturnal atmospheric boundary layer in Kathmandu, Nepal, Atmos. Chem. Phys., 9, 6401–6415, https://doi.org/10.5194/acp-9-6401-2009, 2009.

Zhang, W., Zhu, T., Yang, W., Bai, Z., Sun, Y. L., Xu, Y., Yin, B., and Zhao, X.: Airborne measurements of gas and particle pollutants during CAREBeijing-2008, Atmos. Chem. Phys., 14, 301–316, https://doi.org/10.5194/acp-14-301-2014, 2014.

Zhang, Y., Du, W., Wang, Y., Wang, Q., Wang, H., Zheng, H., Zhang, F., Shi, H., Bian, Y., Han, Y., Fu, P., Canonaco, F., Prévôt, A. S. H., Zhu, T., Wang, P., Li, Z., and Sun, Y.: Aerosol chemistry and particle growth events at an urban downwind site in North China Plain, Atmos. Chem. Phys., 18, 14637–14651, https://doi.org/10.5194/acp-18-14637-2018, 2018.

Zhu, Y., Zhang, J., Wang, J., Chen, W., Han, Y., Ye, C., Li, Y., Liu, J., Zeng, L., Wu, Y., Wang, X., Wang, W., Chen, J., and Zhu, T.: Distribution and sources of air pollutants in the North China Plain based on on-road mobile measurements, Atmos. Chem. Phys., 16, 12551–12565, https://doi.org/10.5194/acp-16-12551-2016, 2016.